ALMA MATER STUDIORUM · UNIVERSITÀ DI BOLOGNA

Scuola di Scienze

Corso di Laurea Magistrale in Fisica

Cyclotron production of ^{11}C: experimental assessment of saturation yield and validation with Monte Carlo simulation

Relatore:

Prof.ssa Maria Pia Morigi

Correlatori:

Dott. Mario Marengo
Dott. Federico Zagni
Ing. Angelo Infantino

Presentata da:

Andrea Chiappiniello

Sessione II

Anno Accademico 2013/2014

Abstract

Nell'ambito della Fisica Medica, le simulazioni Monte Carlo sono uno strumento sempre più diffuso grazie alla potenza di calcolo dei moderni calcolatori, sia nell'ambito diagnostico sia in terapia. Attualmente sono disponibili numerosi pacchetti di simulazione Monte Carlo di carattere *general purpose*, tra cui Geant4.

Questo lavoro di tesi, svolto presso il Servizio di Fisica Sanitaria del Policlinico "S.Orsola-Malpighi", è basato sulla realizzazione, utilizzando Geant4, di un modello Monte Carlo del target del ciclotrone GE-PETtrace per la produzione di ^{11}C. Nel modello sono stati simulati i principali elementi caratterizzanti il target ed il fascio di protoni accelerato dal ciclotrone.

Per la validazione del modello sono stati valutati diversi parametri fisici, tra i quali il range medio dei protoni nell'azoto ad alta pressione e la posizione del picco di Bragg, confrontando i risultati con quelli forniti da SRIM. La resa a saturazione relativa alla produzione di ^{11}C è stata confrontata sia con i valori forniti dal database della IAEA sia con i dati sperimentali a nostra disposizione.

Il modello è stato anche utilizzato per la stima di alcuni parametri di interesse, legati, in particolare, al deterioramento dell'efficienza del target nel corso del tempo. L'inclinazione del target, rispetto alla direzione del fascio di protoni accelerati, è influenzata dal peso del corpo del target stesso e dalla posizione in cui questo è fissato al ciclotrone. Per questo sono stati misurati sia il calo della resa della produzione di ^{11}C, sia la percentuale di energia depositata dal fascio sulla superficie interna del target durante l'irraggiamento, al variare dell'angolo di inclinazione del target.

Il modello che abbiamo sviluppato rappresenta, dunque, un importante strumento per la valutazione dei processi che avvengono durante l'irraggiamento, per la stima delle performance del target nel corso del tempo e per lo sviluppo di nuovi modelli di target.

Contents

Introduction

Nuclear medicine, a medical specialty involving the application of radionuclides in the diagnosis and treatment of disease, is a constantly growing sector. The *positron emission tomography* (PET) has an important role in diagnostic imaging. The standard radionuclides used in PET imaging are ^{11}C, ^{13}N, ^{15}O and ^{18}F, which are produced by cyclotron irradiation of liquid or gaseous targets. Several radiopharmaceuticals, obtained from synthesis of these radionuclides, such as ^{18}F-FDG (fludeoxyglucose) and ^{11}C-choline, are used for the detection and staging of various tumors, others, such as ^{13}N-ammonia and H$_2^{15}$O, are, respectively, the optimal tracers for the study of myocardial perfusion phenomena and blood flow.

The developments of medical physics instrumentation and the availability of ever more powerful computing systems have led to an increasing use of *Monte Carlo* techniques in this field, both in diagnostics and in therapy. Monte Carlo modeling is, in fact, a powerful tool which is currently used for the design and optimization of several instrumentation in this field, including radiation detectors, imaging and radio-protection devices.

Currently, many *general purpose* Monte Carlo platforms are available, such as Geant4, a toolkit developed at CERN and widely used. Geant4 was originally designed for the high-energy physics experiments, but has found several applications outside this domain in the areas of medical and biological sciences, radiation protection and astronautics.

The purpose of this thesis, which was conducted at the Medical Physics unit of the Bologna University Hospital "S. Orsola-Malpighi", is to develop the Monte Carlo model, using Geant4, of the target for the production of ^{11}C of the GE PETTrace cyclotron. The model was validated through known and experimental physical parameters in order to assess its accuracy. The model of the target establishes, in fact, a powerful tool for a number of applications and studies regarding the performance and

behavior of the target during irradiation. An example, which will be discussed in this thesis, is the estimation of the activation and energy distribution on the internal wall of the target, which may affect the observed lowering of target performance over time. Moreover, to my knowledge, there are very few applications of the Geant4 toolkit to biomedical cyclotron devices, which involves the simulation of such low-energy hadronic interactions. For this reason, this work also constitutes an interesting test for this Monte Carlo code in this field.

In the first chapter the radionuclides of medical interest, with particular reference to positron emitters radionuclides for PET tomography, the cyclotron physics, and the characteristics of the GE PETtrace cyclotron, with reference to the ^{11}C target, will be described.

The theory for the calculation of the target activation, by irradiation with charged particles, will be explained in the second chapter.

In the third chapter the theory of Monte Carlo techniques will be introduced, with reference to simulations in Nuclear Medicine, drawing attention to Monte Carlo platforms currently available for physics applications. The second section of this chapter is devoted to the description of the global structure of Geant4 and the architecture of a simulation with this toolkit, from the definition of the geometry, the sources and detectors, to the output management.

The Geant4 simulation of the ^{11}C target is the subject of the fourth chapter. Here it is described the target geometry and the source modeling, the physics models that are used to describe the processes which occur in the target, and how the data of interest are extracted and analyzed. In an initial set of simulations, aimed to find the optimal parameters of the Physics List to be used, a simplified geometry was utilized.

In the fifth and last chapter the results of interest, obtained from the simulated model, and their validation by means of the comparison with values which are obtained experimentally or through a validated toolkit (SRIM) will be presented.

Finally, conclusions and hypothesis of future work are exposed.

Chapter 1

Cyclotron in the medical field

1.1 Radionuclides of medical interest

Radiopharmaceuticals are drugs that include one or more radionuclides and are used in the field of nuclear medicine as tracers in the diagnosis and treatment of many diseases. Radiopharmaceuticals incorporate a radioactive tracer nuclide into a metabolically-active molecule; once it has been administered in the patient's body, the radionuclide tracer atom allows it to be detected with an imaging device. A radiopharmaceutical can be used both in diagnostic and therapy field, and it is characterized, in addition to the chemical structure and the pharmaceutical form, also by the radionuclide used, from the properties of which depends not only the possibility of synthesis of the radio-pharmaceutical and its stability, but also the efficiency of detection and the radiation exposure of the patient. Therefore, the ideal characteristics of a radionuclide used for the preparation of a radiopharmaceutical are:

- short half-life;

- decay into a stable nuclide;

- high specific activity;

- high radionuclidic purity;

- low cost of production;

- ready availability;

- type of emitted radiation, according to the intended use;

- chemical aptitude of binding with biological molecules of interest.

1.1.1 Radioactive Decay

Radioactive decay is the process by which a unstable nucleus of an atom (radionu-clide) loses energy by emitting ionizing radiation. A material is considered radioactive if spontaneously emits this kind of radiation, which includes the emission of *alpha* particles, *beta* particles, *gamma rays* and other subatomic particles.[1]

In α-decay an atomic nucleus emits an α particle (a nucleus of ^{4}He) and thereby transforms into an atom with a mass number 4 less and atomic number 2 less:

$$^A_Z X \rightarrow\, ^{A-4}_{Z-2}Y + \alpha \tag{1.1}$$

Alpha-decay typically occurs in the heaviest nuclides. The α particles have a very high LET (*Linear Energy Transfer*) and therefore are not very penetrating: they are shielded by a few centimeters of air or a piece of paper.

β-decay is a type of radioactive decay in which a β particle (an electron e^- or a positron e^+) is emitted from an atomic nucleus. This process allows the atom to obtain the optimal ratio of protons and neutrons. There are two subtypes of beta-decay: beta minus and beta plus. In β^- decay, the weak interaction converts an atomic nucleus into a nucleus with one higher atomic number while an electron e^- and an electron antineutrino $\bar{\nu}_e$ are emitted. The generic equation is:

$$^A_Z X \rightarrow\, ^A_{Z+1}Y + e^- + \bar{\nu}_e \tag{1.2}$$

In β^+ decay the weak interaction converts a nucleus into its next-lower neighbor on the periodic table while a positron e^+ and an electron neutrino ν_e are emitted. The generic equation is:

$$^A_Z X \rightarrow\, ^A_{Z-1}Y + e^+ + \nu_e \tag{1.3}$$

Sometimes *electron capture* is included as a type of beta-decay, because the basic process, mediated by the weak force is the same, however no β particle is emitted. In all cases where β^+ decay of a nucleus is allowed energetically, the electron capture process is also allowed; in this process an inner atomic electron is captured in the nucleus by a proton that "becomes" a neutron, with the emission of an electron neutrino ν_e:

$$^A_Z X + e^- \rightarrow\, ^A_{Z-1}Y + \nu_e \tag{1.4}$$

The beta-decay changes, therefore, the atomic number of the daughter nuclide keeping constant the mass number. The β particles are little penetrating, although more than α particles, and are usually stopped by a few meters of air or by few millimeters of aluminum.

Nuclear isomers, metastable states of atomic nucleus caused by the excitation of one or more of its nucleons, undergo gamma decay. In γ-decay a nucleus changes from a higher energy state to a lower energy state through the emission of photons:

$$\,^{A}_{Z}X^{m} \rightarrow \,^{A}_{Z}X + \gamma \tag{1.5}$$

The number of protons and neutrons in the nucleus does not change in this process, so the parent and daughter atoms are the same chemical element. Metastable isomers may also decay by *internal conversion*, a process in which the energy of nuclear de-excitation is not emitted as γ rays, but instead used to accelerate one of the inner electrons of the atom, so that it gains high kinetic energy. This result occurs because inner atomic electrons penetrate the nucleus, where they are subject to the intense electric fields which result when the protons of the nucleus re-arrange in a different way.

Often, after a α or β decay, the daughter nuclide is in an excited state and tends to move to a more stable energy level by the emission of a γ photon. These photons are usually very energetic and penetrating. Their LET, for the same energy, in fact it is much less than that of the massive particles. They are stopped by large thicknesses of lead or concrete.

In nuclear medicine, the radionuclide used par excellence is ^{99m}Tc, a well-known nuclear isomer which decays by emitting a photon of 140 keV of energy (used for single photon imaging) with half-life of about 6 hours. ^{99m}Tc is produced by a ^{99}Mo-^{99m}Tc generator that guarantees optimal availability. Since it is not a beta emitter, the irradiation of the patient is limited.

Main positron-emitting radionuclides used in PET investigations are:

- fluorine-18, that decays into ^{18}O ($T_{1/2}$=109.77 min);

- oxygen-15, that decays into ^{15}N ($T_{1/2}$=2.037 min);

- nitrogen-13, that decays into ^{13}C ($T_{1/2}$=9.97 min);

- carbon-11, that decays into ^{11}B ($T_{1/2}$=20.39 min).[2]

1.1.2   PET

PET (*positron emission tomography*) is a nuclear medicine imaging technique that produces a 3-D image of functional processes in the body. The system detects pairs of annihilation photons emitted indirectly by a positron-emitting radionuclide (*tracer*), which is introduced into the body bound to a biologically active molecule (*radiopharmaceutical*). Three-dimensional images of tracer concentration within the body are then evaluated through a reconstruction algorithm. In modern PET-CT scanners, functional PET imaging is coupled to a CT scan, performed on the patient during the same session and in the same machine, to provide anatomical information.
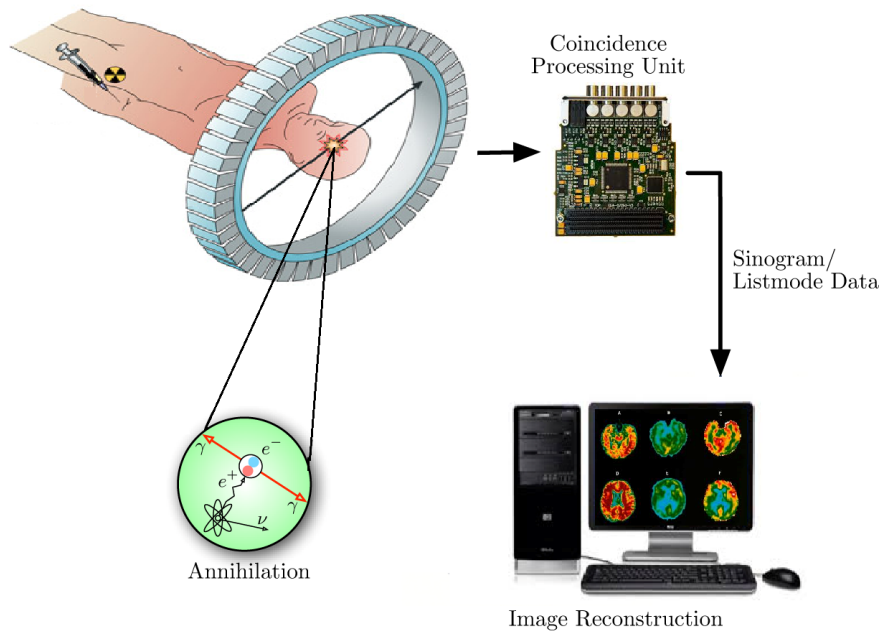

Figure 1.1: Scheme of a PET acquisition process.

As the radioisotope undergoes β^+ decay, it emits a positron that travels in tissue for a short distance (the mean free path of the positron annihilation first is a function of its energy and the atomic number of the absorbing material, and is generally between 0.1 and 0.5 mm), during which it loses kinetic energy, until it decelerates to a point where it can interact with an electron. The positron and electron annihilate and it is produced a pair of annihilation photons, each having energy equal to the rest mass of the electron, moving in approximately opposite directions. Since momentum of the system is not always equal to zero, there may be deviations in the direction of emission of the photons ($180° \pm 0.25°$). Around the patient is placed a detection

system, composed of scintillators and photomultipliers, to reveal the pairs of photons emitted.
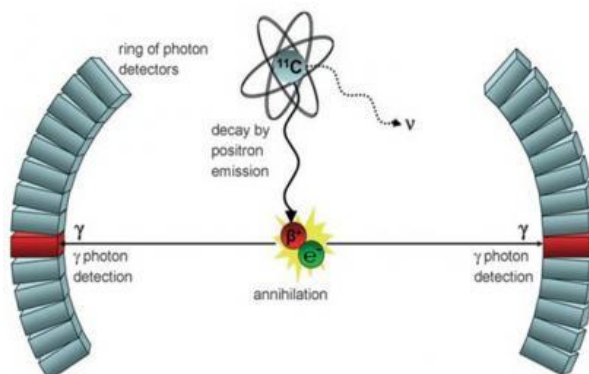

Figure 1.2: Electron-positron annihilation and revelation of the pair of annihilation photons by the detection system.

Two detectors placed in opposition allow to detect the two photons in coincidence (if they fall within a predetermined time window). It can therefore identify the line of response (LOR) along which the position of annihilation is located. The photons are much more energetic than conventional nuclear medicine which makes use of ^{99m}Tc: then scintillation crystals with higher effective atomic number and/or thicker than in gamma cameras are required. In order to detect photons in coincidence, a high speed of light emission is also fundamental.

The table 1.1 shows the physical properties of the scintillation crystals commonly used in PET (sodium iodide activated with thallium, NaI(Tl), is reported for comparison, due to its high light yield). BGO (*bismuth germanate*, $Bi_4Ge_3O_{12}$) has a higher effective atomic number than NaI(Tl), but a lower light yield. LSO(Ce) (*Cerium-doped lutetium oxyorthosilicate*, Lu_2SiO_5) and LYSO(Ce) (Cerium-doped lutetium-yttrium oxyorthosilicate) compared to BGO have lower decay constants and higher light yields. They have the drawback of radioactivity traces, which represent background noise, but time-of-flight (TOF) PET image reconstruction algorithms allow to obviate this. GSO (Gadolinium oxyorthosilicate, Gd_2SiO_5) is another material used in PET tomography: its characteristics are similar to those of LSO, but GSO has a lower light yield.

The most common radiopharmaceutical employed in PET imaging is ^{18}F-FDG (fludeoxyglucose), a glucose analogue, in which a -OH group (hydroxide) is substituted with ^{18}F. The tracer concentrations will indicate tissue metabolic activity by

	NaI(Tl)	BGO	LSO(Ce)	LYSO(Ce)	GSO
Density (g/cm^3)	3.67	7.13	7.40	5.37	6.7
Effective atomic number (Z)	51	75	65	54	59
Light yield (% NaI)	100	15	75	75	30
Index of refraction	1.85	2.15	1.82	1.81	1.85
Peak wavelength (nm)	410	480	420	420	430
Decay constant (ns)	230	300	40	53	60
Attenuation length (mm)	29.1	10.4	11.4	20.0	14.1

Table 1.1: Examples of scintillators and their properties.[3]

virtue of the regional glucose uptake. The use of this tracer to explore cancer staging is the most common type of PET scan in standard medical care, however, many other radioactive tracers are used in PET to image the tissue concentration of other types of molecules of interest. The main radionuclides used in PET diagnosis, already mentioned at the beginning of the section, can be produced by a cyclotron.[1]

1.2 Cyclotron

1.2.1 Introduction

A particle accelerator is a machine that produces beams of charged particles with high kinetic energy. The first accelerators used static electric fields to accelerate particles, but electrical breakdown limits the achievable kinetic energy for particles in these devices. The need to accelerate particles to higher potential differences led to the creation of the first linear particle accelerators (LINAC) that greatly increases the velocity of charged particles by subjecting the charged particles to a series of oscillating electric potentials along a linear beamline. This method of particle acceleration was invented by Leó Szilárd and was patented in 1928 by Rolf Widerøe, who, influenced by a publication of Gustav Ising, also built the first operational device.

Linear accelerators use a linear array of drift tubes to which an alternating electric field is applied. As the particles approach a tube, they are accelerated towards it by an opposite polarity charge applied to the tube. When they pass through a hole in the tube, the polarity is switched so that now the plate repels them and they are
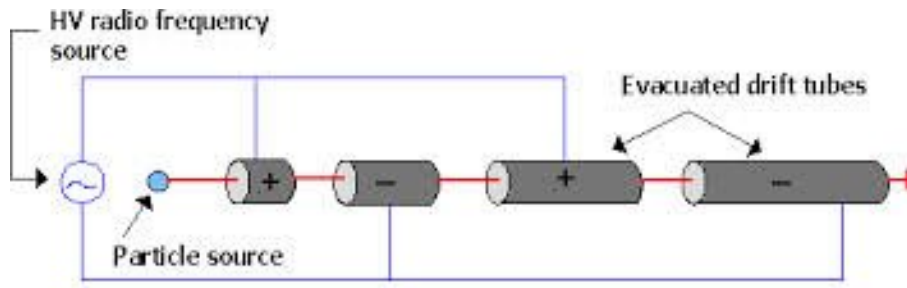
Figure 1.3: Scheme of a linear accelerator.

accelerated by it towards the next tube. As the particles approach the speed of light, the switching rate of the electric fields becomes so high that they operate at radio frequencies, and so microwave cavities are used in higher energy machines instead of simple drift tubes.

In the 1920s, it was not possible to generate the high intensity and high-frequency radio waves which are used in modern Linear Accelerators. Thus unrealistic long LINAC structures were required for higher-energy particles. The compactness of cyclotrons solves this problem reducing heavy costs, such as construction, radiation shielding, and the enclosing building. Cyclotrons have a single electrical driver which saves both money and power. Furthermore, cyclotrons are able to produce a continuous stream of particles at the target, so the average power passed from a particle beam into a target is relatively high.

Ernest Lawrence invented and patented the cyclotron that became operational in 1932, with the important contribution of a graduate student, M. Stanley Livingston. In a cyclotron the particles are held to a spiral trajectory by a static magnetic field and accelerated by a rapidly varying electric field. Inside a circular vacuum chamber there are two semicircular hollow electrodes (called "dees" because of the shape). These electrodes can be affected by spurious particles that cause the heating and must be cooled by circulation of water in special tubes. The chamber is placed between the polar parts of a powerful magnet, so that the field crosses the plane on which the electrodes lie. When a particle is introduced tangentially to the chamber, perpendicularly to the magnetic field, it is diverted and maintained on a circular orbit due to the Lorentz force. If then a suitable high-frequency alternating voltage is applied between the two electrodes, the particles undergo an acceleration whenever they pass into the space between them. Accelerating, the orbit diameter increases, until the beam emerges
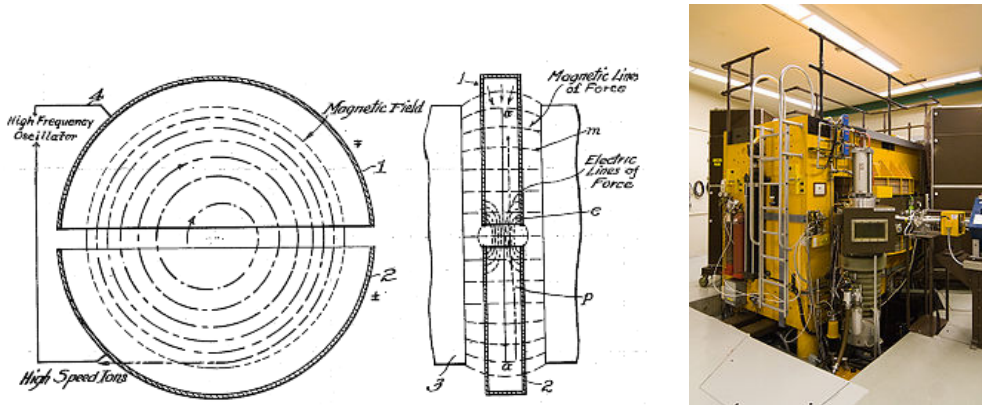
9

tangentially from the edge of the device.

Figure 1.4: On the left, diagram of cyclotron operation from Lawrence's 1934 patent. The "D" shaped electrodes are enclosed in a vacuum chamber, which is installed in the gap between the two poles of a magnet. On the right, example of modern cyclotron.

Lawrence won the Nobel Prize in Physics in November 1939 "for the invention and development of the cyclotron and for results obtained with it, especially with regard to artificial radioactive elements". As well as for the discovery of transuranic elements, the cyclotron was immediately used in the medical field.[4]

1.2.2   The physics

A charged particle subjected to a uniform electric field E accelerates like:

$$a = \frac{F}{m} = \frac{qE}{m} \tag{1.6}$$

and there is a variation of its kinetic energy:

$$\Delta K = q\Delta V \tag{1.7}$$

where ΔV is the potential difference.
The centripetal force that keeps the particles in the circular trajectory is generated by the transverse magnetic field B, due to the Lorentz force. In this case, the centripetal force is:

$$\frac{mv^2}{r} = qvB \tag{1.8}$$

where m is the mass of the particle, q is the charge, v is the velocity and r is the radius of the trajectory.

From the eq. 1.8 we can derive r, the radius of the circular trajectory:

$$r = \frac{mv}{qB} \tag{1.9}$$

and the rotation frequency ν:

$$\nu = \frac{\omega}{2\pi} = \frac{1}{2\pi}\frac{v}{r} = \frac{qB}{2\pi m} \tag{1.10}$$

where ω is the angular velocity. It can be seen that, in the non-relativistic approximation, the frequency required is independent of the radius of the orbit. With the increase of the speed of the particle, this approximation is no longer valid and the frequency is no longer constant: we must consider, in fact, the relativistic mass that increases as particles approach the speed of light. As their relativistic mass increases, modifications to frequency (synchrocyclotron) or to magnetic field are required during the beam acceleration (isochronous cyclotron). We can write the relativistic mass as:

$$m = \frac{m_0}{\gamma} = \frac{m_0}{\sqrt{1-\beta^2}}, \qquad \beta = \frac{v}{c} \tag{1.11}$$

So the relativistic cyclotron frequency can be written as:

$$\nu = \frac{qB}{2\pi\gamma m_0} = \frac{\nu_0}{\gamma} \tag{1.12}$$

To be sure that the particles are always accelerated (resonance condition), the source of radio-frequency must reverse the polarity of the electrodes whenever the charged particles pass between them. To observe the resonance condition, the radio frequency ν_{RF} must be an integer multiple of the cyclotron frequency ν_c:

$$\nu_{RF} = h\nu_c, \qquad h = 1, 2, .. \tag{1.13}$$

where h is the number of harmonic.

Referring to a cyclotron as in fig. 1.5, the ions are accelerated in the four gaps between the electrodes. H^- ions are accelerated in the first harmonic, hence a difference of potential is applied in phase opposition to the two resonators and the beam gets four accelerations in a full circle (in this case it is possible to accelerate only a packet of particles at a time). D^- ions are accelerated in the second harmonic, hence a ddp is applied in phase to the two resonators and then they get two accelerations (in this case it is possible to accelerate two packets of particles simultaneously).

An evolution of cyclotron is the synchrocyclotron, patented by Edwin McMillan, in which the frequency of the RF electric field is varied to compensate relativistic effects. A further evolution of the synchrocyclotron is the synchrotron, where the radius is constant and the electric and magnetic fields are variable.
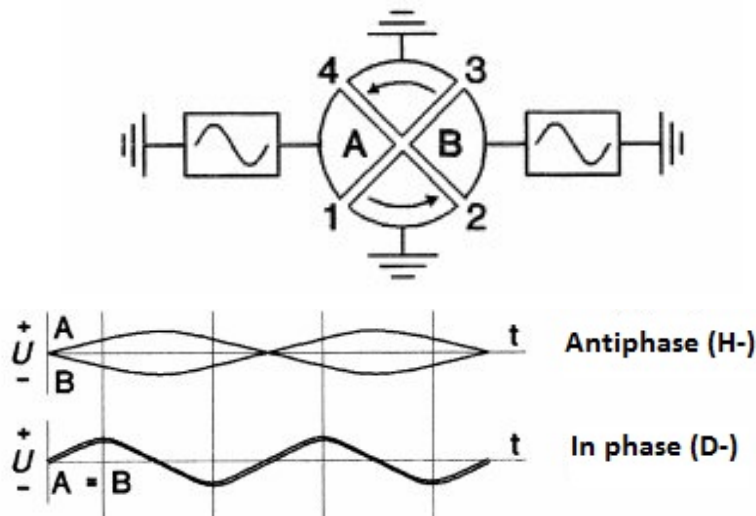
Figure 1.5: At the top is shown a simple scheme of a cyclotron , where there are four electrodes, two "real" (A, B) connected to the source of radio-frequency and two "false" connected to the ground. Below the first two harmonics allowed are shown.
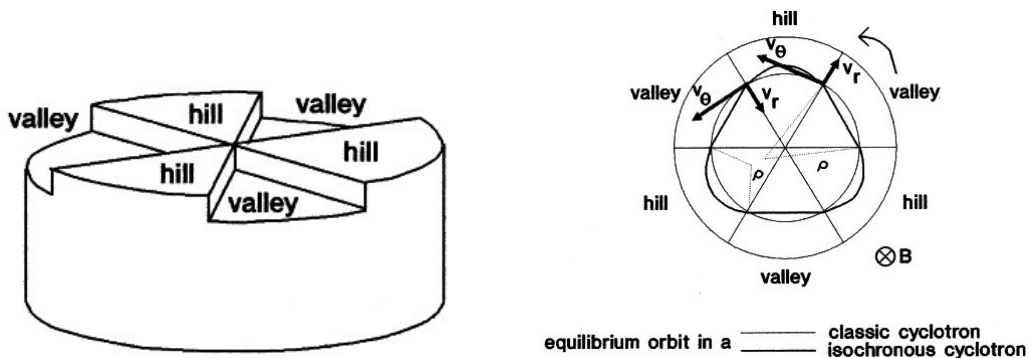
1.2.3 Isochronous cyclotron

Figure 1.6: On the left, magnet of an isochronous cyclotron with three *valleys*. On the right, comparison between the orbits of a traditional and a isochronous cyclotron.

An alternative to the synchrocyclotron is the isochronous cyclotron, which maintains a constant RF driving frequency and compensates relativistic effects by increasing the magnetic field with radius. Isochronous cyclotrons are able to produce much greater beam current than synchrocyclotrons, but require azimuthal variations in the field strength to provide a strong focusing effect and keep the particles captured in their spiral trajectory. The removal of radial sectors by the magnet, as in fig. 1.6, creates the zones with a high gap between the two magnets (*valleys*) and areas with a lower

gap (*hills*). The ions are affected by a strong magnetic field in the *hills* and a weaker one in the *valleys*, i.e. they are subjected to a magnetic field gradient which varies the trajectory compared to that of a conventional cyclotron, as can be seen in fig. 1.6. Ions have a radius of curvature smaller in the *hills* compared to the *valleys*, thus ensuring a focusing of the beam also at relativistic speed.[5]
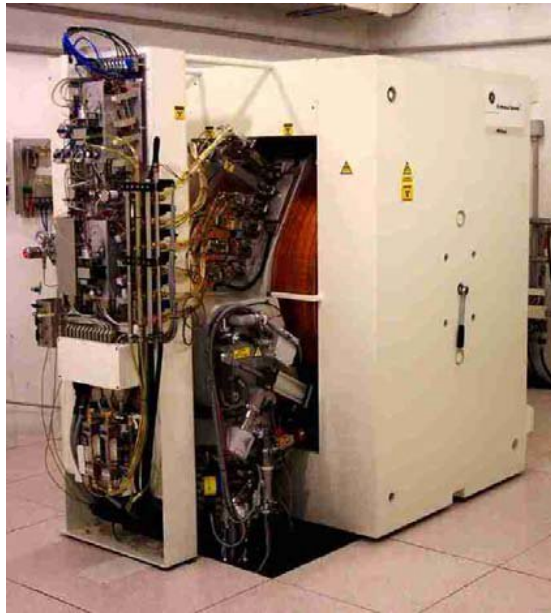
1.3 The GE PETTrace Cyclotron

Figure 1.7: The GE PETTrace Cyclotron.

The PETtrace, manufactured by General Electric Medical Systems and used at the Medical Physics unit of the Bologna University Hospital "S. Orsola-Malpighi", is an isochronous cyclotron that works at fixed energy, able to accelerate negative hydrogen ions (H^-) up to 16.5 MeV and negative ions of deuterium (D^-) up to 8.4 MeV, with a maximum of beam intensity, respectively, of 100 μA and 60 μA (after recent hardware upgrades). The beam of accelerated particles can be directed on one of the 6 output ports available. The cyclotron is equipped with 5 kinds of targets for the production of the main radionuclides of interest for PET (^{11}C, ^{13}N, ^{15}O, $^{18}F^-$, $^{18}F_2$), and is able to operate in a dual beam, i.e. it can radiate simultaneously two targets.[6]

The PETtrace can be divided into several subsystems:

1. Magnets;

2. source of radio-frequency;

3. ion source;

4. extraction system of the beam;

5. control system of the beam;

6. vacuum system;

7. targets.
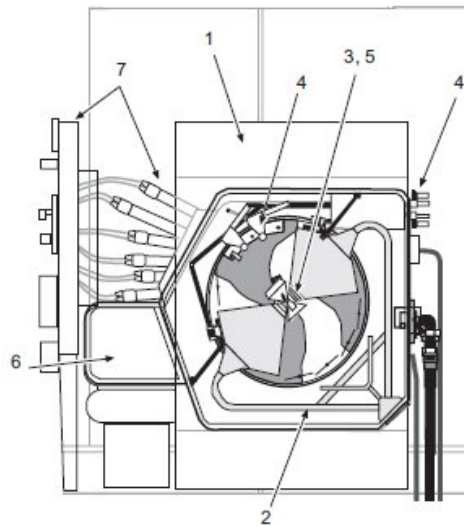
Figure 1.8: GE PETtrace subsystems, numbered as in the list above.

1.3.1 The magnets

The bearing structure of the magnets is of standard industrial steel with low content of carbon (<0.18%); the poles of the magnet, that are also of steel with a low carbon content (<0.05%), are a single piece forged. The poles of the magnet are divided into two different areas, the *hills* and *valleys* (the *valleys* are created by removing radial sectors of the magnet), as can be seen in fig. 1.9. The magnetic field is induced by copper hollow conductors inside which circulates demineralized water for refrigeration. The magnet is oriented vertically.

Figure 1.9: Ge PETtracer magnets.

1.3.2 The source of radio-frequency

The particles are accelerated by the radiofrequency system that is connected to two of the 4 *dees* present, which are placed at an angle of 75°; the other two *dees* are connected to the ground. The negative hydrogen ions are accelerated in the first harmonic in order to be accelerated to 4 times for each revolution, while the deuterium ions are accelerated in the second harmonic and get two accelerations for each revolution. The mass difference between the two types of particles that the cyclotron is capable of accelerating, in addition to affect the intensity of the magnetic field to be applied, determines a different choice of the frequency of oscillation (27.2 MHz for H^- ions, 27.8 MHz for D^- ions), that are generated by the RFPG (*Radio Frequence Power Generator*, placed outside the bunker in which the cyclotron is installed) connected to the electrodes via a coaxial cable (*RF Feeder Cable*) which transmits radio-frequency.

1.3.3 The ion source

The ion source is located in the center of the cyclotron and it is a cold-cathode-type PIG (*Penning ion gauge*) source. The ion source contains in its interior two separate chimneys, one for the production of H^- and the other for the D^-. The method with which the ions are produced is the same for the two types of particles. Inside a cylindrical chamber there is the electrical discharge produced by a huge electric tension applied between the anode (side surface of the cylinder), connected to the ground, and two cathodes (bases of the cylinder), to which is applied a negative voltage generated by the PSARC (*Power Supply Ion Source*). The plasma of ions and electrons which

15

is created remains confined inside the chamber for the presence of the magnetic field. On one side of the chamber there is a small slit. The ions H^- and D^- come out from the chamber when a positive voltage is applied to the *dee* which is located close to the slit. The slits for the two types of particles are located at opposite positions. The H^- are extracted from the *dee* mounted in the lower part of the cyclotron, while the D^- are extracted in the upper part.

1.3.4 The extraction of the beam

The extraction of the beam is based on the technique of the *stripping foil*. The two electrons of the H^- and D^- ions are stripped during the passage of the beam through a thin foil of carbon (3 μm thick). The charge of the accelerated particles changes from negative to positive, involving a change of the direction of rotation of the beam. The electrons collected by the foil allow a constant monitoring of the beam current. The PETtrace is equipped with two extraction units each of which can extract the beam to three of the six output ports. The extraction units slide on a curved track mounted along the radius of extraction. Each unit contains 6 carbon foils mounted on a revolver which, rotating on itself, is able to change the carbon foil when this is damaged. Having two extraction units allows the PETtrace to operate in dual beam (it is possible to irradiate two targets simultaneously). The technique of *stripping foil* allows an efficiency of extraction of the beam equal to 100%.

1.3.5 The control system of the beam

The cyclotron is provided with various monitoring systems of the beam current, both in the vacuum chamber and on the targets. The system includes a *retractable probe* positioned at a small radius of the orbit of acceleration, the *stripping foil*, two *collimators* and the body of the target. All these systems are isolated from the ground to allow a correct measure of current. The tantalum *probe* is located in the proximity of the ion source and it is used at the beginning of irradiation to set the optimal current for the production of the radioisotope. A correct reading of the current in this phase of irradiation allows to control that the accelerator and the various subsystems are functioning properly. The *foils*, in addition to changing the direction of rotation, allow a constant monitoring of the beam intensity, measuring the current created by

the electrons extracted from the negative accelerated ions. The collimators are placed on the inner part of the output ports. They are also in tantalum or graphite and are used to center the beam, cutting each non-aligned tail. Also the body of the target is isolated from the ground to allow the measure of the effective current present on the target material during the production of radioisotopes. All the signals useful for the monitoring of the beam are connected to the multichannel BCA (*Current Beam Analyzer*).
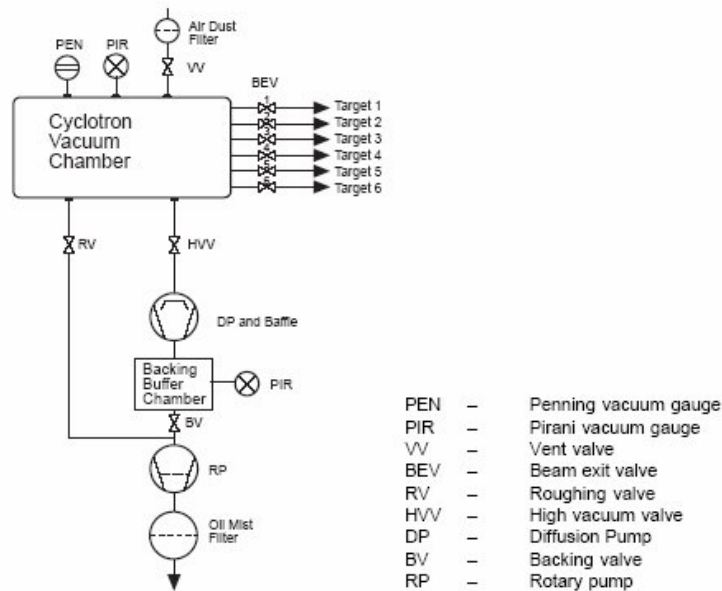
1.3.6 The vacuum system

Figure 1.10: Diagram of the system to produce the vacuum.

Since the binding energy of the second electron in a hydrogen atom is very low (0.755 eV), it is therefore essential, in order to accelerate negative ions, to create high-vacuum inside the cyclotron, about an order of magnitude more than in a cyclotron that accelerates positive ions [7]. The vacuum is made with the aid of two pumps, a *rotary pump* to generate the pre-vacuum and a *diffusion pump* to bring the vacuum inside the chamber in optimum working conditions. The pumps are connected to the acceleration chamber of the cyclotron through a *high-vacuum valve*. To measure the wide range of pressure inside the vacuum chamber are installed two pressure switches: the *Pirani pressure switch*, capable of measuring pressures from 1 bar to 10^3 mbar and

the *Penning pressure switch* for the measurement of high vacuum ($< 10^3$ mbar).

Constant pressure without gas flow (pressure reached after 48 h)	$5 \times 10^{-7} \pm 2 \times 10^{-7}$ mbar
Pressure reached after 1 h ($P_{t=0} = 1$ atm)	6×10^{-6} mbar
Pressure during irradiation ($\phi = 5$ sccm/min)	4×10^{-5} mbar
Pump capacity	2600 l/s

Table 1.2: Specifications in normal working conditions.

The vacuum system is fully automated and controlled by the VCU (*Vacuum Control Units*), that constantly works.
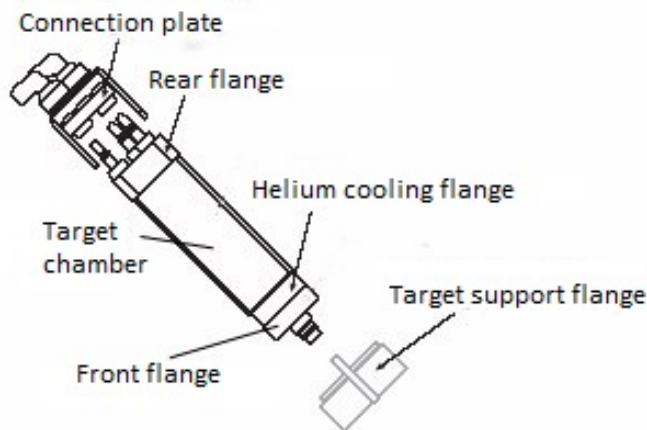
1.3.7 The targets

Figure 1.11: Structure of a generic target.

The targets, placed at the port of the accelerated beam, are the subsystems that contain the irradiation target material. The particle beam hits and transfer its energy to the target material and thus the nuclear reactions (required for the radionuclides production) take place. The cyclotron GE PETtrace is equipped with 5 different types of specific targets for the production of the main radioisotopes of PET interest. Each target is formed by a front flange for the connection to the cyclotron, a flange for cooling with Helium, a chamber where there is the target material and a rear flange for connection to the different cooling and sorting support.

The front flange guide the target in the correct mounting position; all the targets are easy to install and remove with a lever, which simplifies operations. The target chamber is separated from the vacuum chamber of the cyclotron by means of two thin Havar^{TM} foils (42.5% Co, 20% Cr, 17.9% Fe, 13% Ni, 2.8% W, 2% Mo, 1.6% Mn, 0.2% C, 0.04% Be), a non-magnetic resistant alloy. During the irradiation, helium circulates between the two Havar^{TM} foils at a pressure of about 0.5 MPa, which allows the cooling of the metallic foils. The target material is generally in liquid or gaseous form. The design and the type of material used for the construction of various targets is made in order to dissipate the heat developed by the interactions, to withstand the intense radiation beam to which the whole body of the target is subjected and especially to maximize the nuclear reaction of interest. Aluminum is the material used for targets
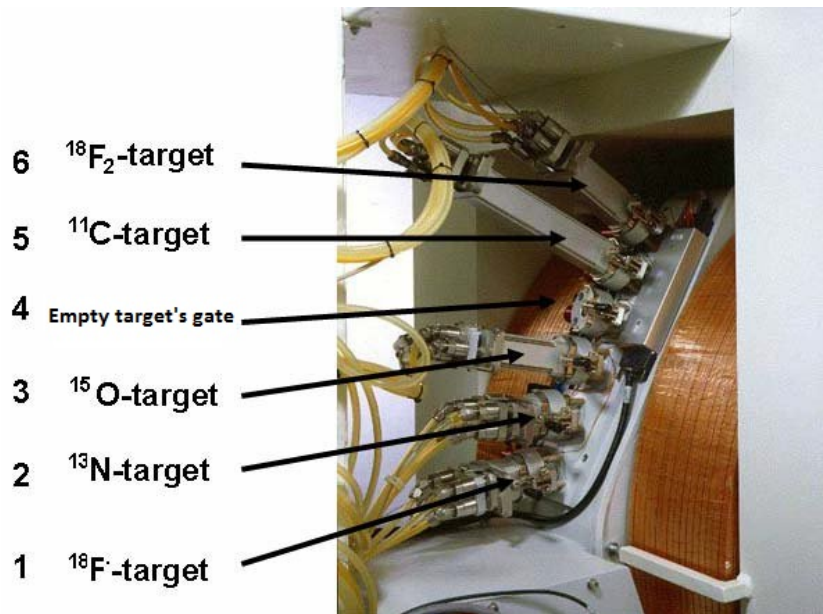

Figure 1.12: Targets installed on the GE PETtrace.

construction. The aluminum is chosen due to the excellent properties of activation of the metal, in fact, the activation products have a short half-life and are relatively few compared to those generated in the other possible metals. The aluminum has a good ductility and a high thermal conductivity (247 W K m^{-1}). All target supports (target material, water to cool the body of the target, helium for cooling the metallic foils) enter and leave the target through the rear flange. Because the target is made up of several pieces assembled together is vital to be able to ensure the seal. The seal is obtained by interposing rings of plastic material (Viton, resistant up to 170°) or of

metal (Helicoflex) between the surfaces.

Target	Target material	Nuclear reaction	$T_{\frac{1}{2}}$ (min)	Chemical form
^{15}O	N_2 (gas)	^{14}N(d,n)^{15}O	2	^{15}O-O_2
^{13}N	H_2O (liquid)	^{16}O(p,α)^{13}N	10	^{13}N-NO$_x$
^{11}C	N_2+1% O_2 (gas)	^{14}N(p,α)^{11}C	20	^{11}C-CO_2
^{18}F-F$^-$	H_2^{18}O (liquid)	^{18}O(p,n)^{18}F	110	^{18}F-F$^-$
^{18}F-F_2	^{20}Ne+1% F_2 (gas)	^{20}Ne(d,α)^{18}F	110	^{18}F-F_2

Table 1.3: Features of the target installed on the GE PETtrace.

1.4 ^{11}C target

Figure 1.13: Picture of ^{11}C target.

The chamber in which is inserted the target material has a cylindrical shape, it is 25 cm long and it is able to contain a volume of 80 ml of gas. The target material is separated from the vacuum chamber of the cyclotron by two foils of Havar^{TM} that have a thickness of 25 μm. The target is filled by a gas mixture containing 99% N_2 + 1% O_2 at a pressure of 1.34 MPa (194 psi), which allows the complete absorption of the beam inside the chamber. During the irradiation, the pressure of the target increases up to approximately 3.1 MPa (450 psi). The heat developed by the interaction between the beam and the gas is dissipated from cooling water, which flows in cylindrical cavities parallel to the chamber inside which nuclear reactions take place.[8]

An example of ^{11}C medical use is the ^{11}C-choline, a positron emitting radiopharmaceutical in which a methyl group includes a ^{11}C nuclide. It is used in PET imaging for visualize prostate and brain cancers, given that the cancer cells, which rapidly proliferate, are characterized by a greater uptake of choline, a constituent of membrane phospholipids.
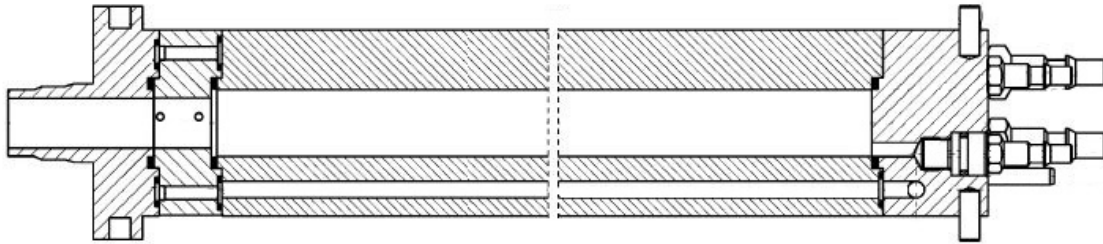

Figure 1.14: Scheme of ^{11}C target.[6]

Chapter 2

Production of radionuclides by irradiation with charged particles

2.1 Nuclear reactions

A nuclear reaction is a process in which two nuclei, or a nucleus of an atom and a subatomic particle (such as a proton or a neutron) from outside the atom, collide to produce one or more nuclides that are different from the original ones. If a nucleus interacts with another nucleus or particle and then they separate without changing the nature of any nuclide, the process is simply referred to as a type of nuclear scattering, rather than a nuclear reaction (in our discussion we will include scattering in nuclear reactions). It is usually used the following notation:

$$A(a,b)B \qquad (2.1)$$

where A is the target, a is the incident particle, B is the product and b is the particle emitted. The main types of reactions are:

- *elastic scattering*: if $b = a$ and $B = A$, there is diffusion due to diffraction nuclear. In this case the wavelength of the incident particle interacts with that of the nucleus before the particle enters inside the nucleus. This process involves only a deflection of the incident particle.

- inelastic scattering: if $B = A^*$, i.e. the product is in an excited state. The incident particle entering the nucleus, excites a nucleon to a higher energy level but retains enough energy to leave the target. The extra energy of the nucleus B

is normally sold off by the emission of a photon, which will then take the nucleus in its ground state.
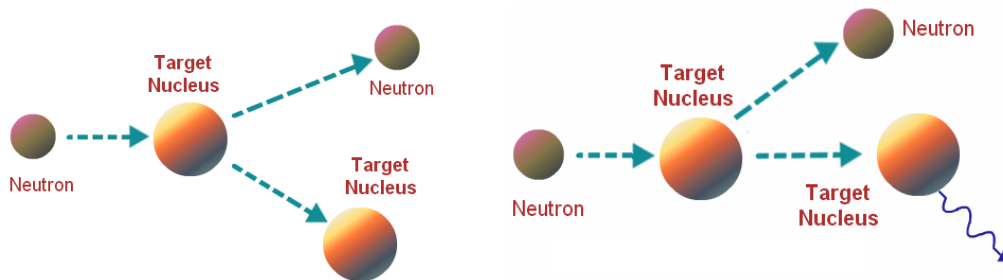
Figure 2.1: Elastic (left) and inelastic (right) scattering.

- *compound nucleus*: if $b \neq a$ and $B \neq A$ there is the formation of a compound nucleus. The incident particle gives so much energy to the target nucleus that is no longer able to leave it. The energy transferred is distributed between the nucleons, until subsequent interactions (collisions) don't lead to focus in a given nucleon sufficient energy to leave the nucleus.

Figure 2.2: Nuclear reaction with the formation of a compound nucleus.

- *thermalization*: if a nucleon is emitted before the incident particle has completely lost its energy. This is an intermediate case between the direct reactions (scattering) and the formation of a compound nucleus.

The probability of a particular nuclear reaction depends on the type and energy of the incident particle and on the target material; more details on this will be provided in the next sections.[9]
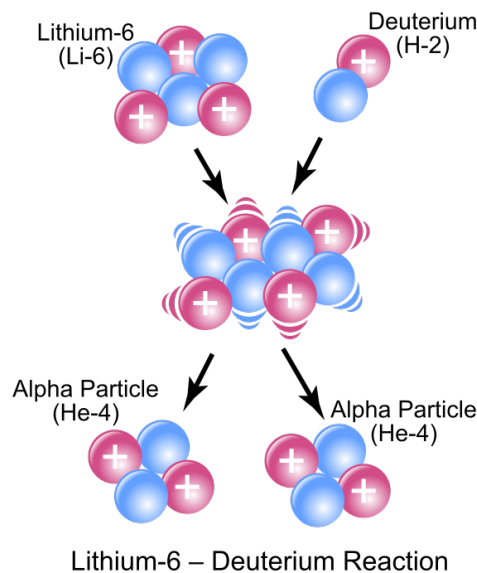
2.1.1 The energy threshold of a reaction

For any type of nuclear reaction:

$$a \,+\, A \rightarrow b \,+\, B \tag{2.2}$$

it is possible to calculate the energy balance, finding:

$$m_a c^2 + K_a + m_A c^2 + K_A = m_b c^2 + K_b + m_B c^2 + K_B \tag{2.3}$$

where K is the kinetic energy and m is the rest mass.

Rewriting the expression above as:

$$(m_a + m_A - m_b - m_B)c^2 = K_B + K_b - K_a - K_A \tag{2.4}$$

it is possible to define the $Q-value$, i.e. the amount of energy released by the reaction:

$$Q = K_b + K_B - K_a - K_A = (m_a + m_A - m_b - m_B)c^2 \tag{2.5}$$

or, if we consider the *binding energies*:

$$Q = BE(b) + BE(B) - BE(a) - BE(A) \tag{2.6}$$

with $BE(X)$ defined, starting from the mass of the nucleus, by its atomic number and its atomic number, as:

$$BE(X_Z^A) = Z \cdot m_p + (A - Z) \cdot m_n - m_X \tag{2.7}$$

where m_p and m_n are respectively the mass of the proton and neutron.

A reaction with a positive Q value is exothermic, i.e. has a net release of energy, since the kinetic energy of the final state is greater than the kinetic energy of the initial state. A reaction with a negative Q value is endothermic, i.e. requires a net energy input, since the kinetic energy of the final state is less than the kinetic energy of the initial state. The reaction will only be possible if the kinetic energy of incident particles is

higher than the threshold. The energy value of the threshold is calculated taking into account the laws of conservation of energy and momentum, and it is:

$$E_{th} = \frac{m_a + m_A}{m_A} \cdot Q \tag{2.8}$$

In case of light particles that collide with heavy nuclei (A>20), the threshold energy is very similar to the module of the Q-value, since the fraction in eq. 2.8 is very close to the unit.[10]

If we consider the reaction of interest:

$$^{14}N + p \rightarrow^{11} C + \alpha \tag{2.9}$$

using the equation 2.6, we obtain:

$$Q = (73439.90 + 28295.67 - 104658.60 - 0.00)\, keV = -2923.03\, keV \tag{2.10}$$

The reaction is endothermic and therefore, to take place, it is necessary that the incident particle has a kinetic energy equal to or greater than:

$$E_{th} = -\left(\frac{(1.009 + 11.011)\, u}{11.011\, u} \cdot 2923.03 \right) keV \approx 3190.88\, keV \tag{2.11}$$

where the masses are expressed in *atomic mass unit.*

With regard to the reaction:

$$^{20}Ne + d \rightarrow^{18} F + \alpha \tag{2.12}$$

we obtain:

$$Q = (137369.20 + 28295.67 - 160644.90 - 2224.57)\, keV = 2795.40\, keV \tag{2.13}$$

The reaction is exothermic, i.e. produces energy. It can always happen, having no energy threshold.

2.2   Nuclear reactions by charged particles

When a beam of charged particles, accelerated to a given energy, interacts with a target, can produce nuclear reactions that lead to the transmutation of nuclei of the target material. In this way it is possible to generate both new stable nuclei and radioactive nuclides. The main reactions of interest, for the production of PET radioisotopes, are those which require the irradiation of targets with protons or deuterons.

2.2.1 Irradiation with protons or deuterons

The main nuclear reactions that can occur, irradiating target materials with protons of kinetic energy below 20 MeV, are:

- $^A_Z X(p,n)^A_{Z+1} Y$

- $^A_Z X(p,2n)^{A-1}_{Z+1} Y$

- $^A_Z X(p,p\,n)^{A-1}_Z Y$

- $^A_Z X(p,\alpha)^{A-3}_{Z-1} Y$

In the (p,n) reactions, for example, the atomic number Z increases by one unit, while the mass number A remains constant: a proton enters the nucleus, and a neutron exits. The result of the reaction is then to change the chemical nature of the element irradiated (there is a change of the atomic number Z), determining a reduction of the ratio $\frac{A}{Z}$ of the total number of nucleons divided by the number of protons. This means that the nuclide product may have an excess of positive charges and therefore will tend to reach a state of equilibrium by a β^+ decay: $^A_Z X \rightarrow\ ^A_{Z-1} Y + e^+ + \nu_e$.

There is an excess of positive charges (with its consequences) also as a result of (p,α) reactions, in wich Z decreases by one unit, but A decreases by two.

Irradiating with deuterons, the main reactions are, instead:

- $^A_Z X(d,n)^{A+1}_{Z+1} Y$

- $^A_Z X(d,2n)^A_{Z+1} Y$

- $^A_Z X(d,\alpha)^{A-2}_{Z-1} Y$

2.2.2 Coulomb barrier

In the case that the particles used to irradiate the target are positively charged, they must overcome the Coulomb repulsion with the target nuclei, also positive, in order to achieve them. The electromagnetic force, which determines the repulsion between charges of the same sign, prevails on the strong nuclear force, which is intensely attractive, up to distances of the order of the atomic radius. For distances greater than the
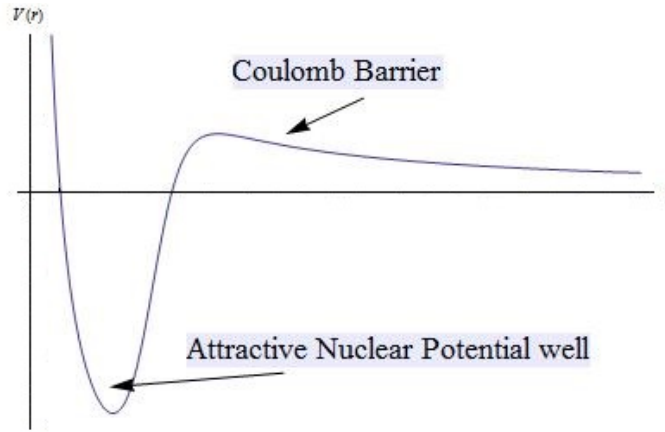
Figure 2.3: Trend of the potential between two nuclei as a function of the distance.

atomic radius (r$\geq$1 fm=10^{-15} m), the incident charge particle is affected only by the Coulomb potential, that is determined by the positive charges of the target nucleus:

$$V(r) = \frac{zZe^2}{r} \tag{2.14}$$

where e is the electron charge (1.602$\cdot$ 10^{-19} C), z is the charge number of the incident particle, Z is the charge number of the target nucleus and r is the distance of the incident particle from the nucleus. Then the force grows as the distance between the incident particle and the target nucleus decreases.

According to classical mechanics, a particle incident can not overcome the Coulomb barrier, if it do not have an energy greater than the repulsive potential; quantum mechanics instead shows that there exists a non-zero probability of crossing even for lower energies (quantum tunneling). It can however be considered that there is a threshold energy below which the probability of penetration is so modest that it can be considered negligible. The minimum kinetic energy necessary to ensure that the incident particle can overcome the Coulomb barrier, starting from the fact that the radius of the nucleus, with reasonable approximation, is proportional to A$^{1/3}$ (the cube root of the mass number), is:

$$E_{min} \approx k \frac{Z_a Z_A}{A_a^{1/3} A_A^{1/3}} \cdot \frac{A_a + A_A}{A_a} \tag{2.15}$$

where Z_a, Z_A2, A_a and A_A are respectively the atomic number and the mass number of the incident particle and of the target nucleus, and k is a proportionality constant ($\approx$1).

28

For light incident particles such as protons or deuterons, the main nuclear reactions of activation are, respectively the (p,n) and (p,α), and the (d,n) and (d,α). In these reactions the transmutation that follows the entrance of the incident particle in the target nucleus leads to the emission of a secondary particle, which is, respectively, a neutron or an alpha particle. With increasing energy of the projectiles, also other types of reactions, such as (p,2n) or, more generally, (p,xn), gradually become more probable.

2.3 Cross section

The atomic nucleus, in a first approximation, can be considered as a well defined sphere, with a radius R, given, with good approximation, by:

$$R \approx r_0 \cdot A^{\frac{1}{3}} \tag{2.16}$$

where r_0=1.2$\cdot$10^{-13} cm and A is the mass number of the nuclide taken into account.[11] Therefore the nucleus provides a transverse section to an incident particle, given by:

$$\sigma_{real} = \pi R^2 \tag{2.17}$$

The interaction of subatomic particles with atomic nuclei, however, can not be considered only as a collision between macroscopic bodies: even nuclear processes and the electrostatic attraction should be considered. Therefore each nucleus provides to incident particles an effective interaction section different from the real one: this effective area is the *cross section*.

The standard unit for measuring nuclear cross sections is the barn, which is defined as:

$$1 \, barn = 10^{-24} \, cm^2 \tag{2.18}$$

Submultiples of the barn, as the *millibarn* (mb), are often used.

The nuclear cross section of a nucleus is used to characterize the probability that a nuclear reaction will occur. Cross sections can be measured for all possible interaction processes together, in which case they are called total cross sections, or for specific processes, such as activation cross section. The cross section of a specific interaction depends on the energy of the incident particle and the type of the target nucleus.
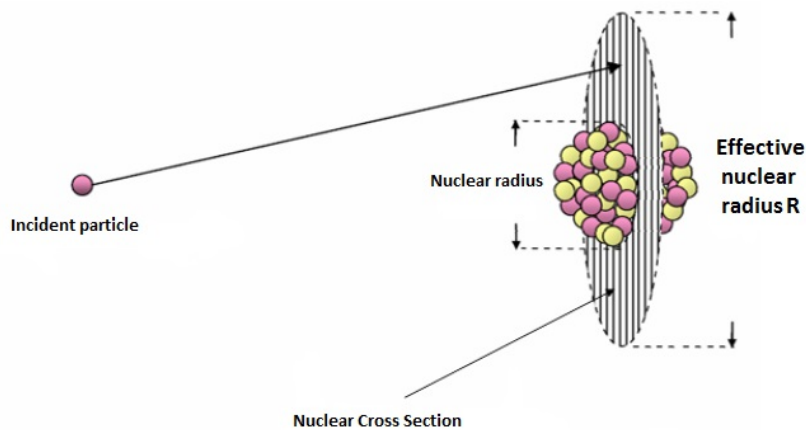
Figure 2.4: Schematic illustration of the concept of cross section.

The theoretical estimates for cross sections reflect the limitations of knowledge about the internal structure of the nucleus, and not always guarantee the desired accuracy for practical purposes. Therefore is usually necessary to refer to the experimental data of the reaction cross sections. The cross sections of the main reactions for production of radionuclides of interest can be found tabulated in various references; an important data collection of radionuclides of biomedical interest was published by the IAEA (*International Agency of Atomic Energy*). These data are derived from an accurate analysis that into account publications related to particularly controlled experimental conditions, and, therefore, they are recommended.
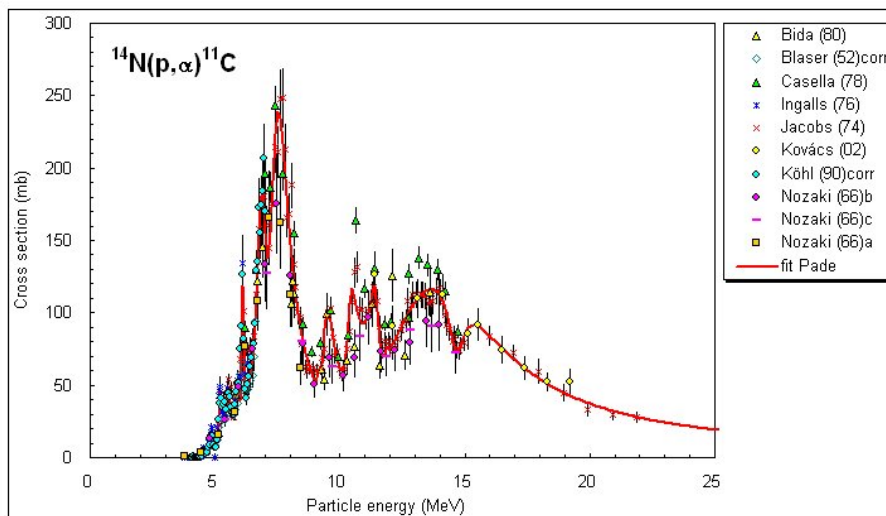

Figure 2.5: Cross sections recommended by the IAEA for the production of ^{11}C with irradiation of protons on a target of ^{14}N.

2.4 Activation of a thin solid target

Consider a particle beam that hits a solid target. If N is the number of nuclear reactions which occur per unit of time and volume in a target thin enough (ΔX) to negligibly change the energy of the particle beam during their passage and so that there is no overlap between the cross sections of the target nuclei, then it is equal to:

$$N = I_p \cdot n_t \cdot \sigma \cdot \Delta X \tag{2.19}$$

where:

- $I_p = \frac{I}{Z}$ is the intensity of incident particles, expressed in particles/sec;

- n_t is the number of target nuclei per cm^3 (unit of volume);

- σ is the cross section, expressed in cm^2.

We can write the number of target nuclei per unit of volume as:

$$n_t = \frac{N_A}{A} \cdot \rho \tag{2.20}$$

where:

- N_A is the Avogadro constant ($6.022 \cdot 10^{23}$ mol^{-1});

- A is the mass number of the target material;

- ρ is the density of the material.

For thin targets, the thickness is frequently expressed in units of mass ($\Delta X \to \rho \cdot \Delta X$), i.e. in g/cm^2; then we can write:

$$N = I_p \cdot \frac{N_A}{A} \cdot \sigma \cdot \Delta X \tag{2.21}$$

The number of nuclei of radioactive material that are present at time t is therefore:

$$N(t) = I_p \cdot \frac{N_A}{A} \cdot \sigma \cdot \Delta X \cdot \int_0^t e^{-\lambda t}\, dt = I_p \cdot \frac{N_A}{A} \cdot \sigma \cdot \Delta X \cdot \frac{1 - e^{-\lambda t}}{\lambda} \tag{2.22}$$

where λ is the decay constant.

The activity, which defines the number of decays in units of time, is then given by:

$$A(t) = \frac{dN(t)}{dt} = I_p \cdot \frac{N_A}{A} \cdot \sigma \cdot \Delta X \cdot (1 - e^{-\lambda t}) \tag{2.23}$$

2.5 Activation of a thick solid target

Each material is characterized by its own *mass stopping power*, defined by:

$$s = \frac{1}{\rho}\frac{dE}{dx} \tag{2.24}$$

where $\frac{dE}{dx}$ is the energy of the incident beam lost per unit path in the target.

The stopping power can be found tabulated for different types of material of interest in several references. For example, an important collection of updated values is available on the website of the NIST (*National Institute for Standards and Technology* [12]). Recalling the definition of mass thickness given in the previous section, the attenuation thickness can be written as a function of energy lost by the beam:

$$\Delta X = \frac{\Delta E}{\frac{1}{\rho} \cdot \frac{dE}{dX}} = \frac{\Delta E}{s} \tag{2.25}$$

In the case of irradiation of a thick target, i.e. that is able to degrade significantly the energy of the beam of incident particles, the equations written in the previous section are no longer valid since the cross section, being a function of energy, has not a constant value. The value that is used in equation 2.23 must be replaced by the integral of the cross section between the initial and final energy of the incident particles. If ΔX is thick enough to degrade the initial kinetic energy of particles (E_0) down to threshold energy for the reaction (E_T) of interest, then the activity can be written as:

$$A(t) = I_p \cdot \frac{N_A}{A} \cdot \int_{E_T}^{E_0} \frac{\sigma(E')}{\frac{1}{\rho}\frac{dE}{dx}(E')} dE' \cdot (1 - e^{-\lambda t}) \tag{2.26}$$

If irradiation time is long enough compared to the half life of the radionuclide produced ($T_{1/2} = \frac{ln(2)}{\lambda}$, i.e. the time in witch half of the atoms decays into another element), the saturation condition is reached, so the exponential term goes to zero and consequently the term in parentheses of the eq. 2.26 becomes equal to 1:

$$A_{sat} = I_p \cdot \frac{N_A}{A} \cdot \int_{E_T}^{E_0} \frac{\sigma(E')}{\frac{1}{\rho}\frac{dE}{dx}(E')} dE' \tag{2.27}$$

i.e. the equilibrium, in which as many new radioactive nuclei are produced as they decay, is reached, and the activity does not increase further. In practical set up, it is useful to make reference to a further quantity, the so called *saturation yield*:

$$Y_{sat} = \frac{A_{sat}}{I} \tag{2.28}$$

where I is the beam current.

The saturation yield is expressed in Bq/A or, more frequently, in mCi/μA. The activity produced by a predefined irradiation system in a given time, can then be evaluated by means of the equation:

$$A(t) = A_{sat} \cdot (1 - e^{-\lambda t}) = Y_{sat} \cdot I \cdot \left(1 - e^{-\frac{ln(2)\cdot t}{T_{1/2}}}\right) \qquad (2.29)$$

thus all fixed characteristics of the production system (physical characteristics of the material irradiated, energy range of the particles, integral of the cross section) are incorporated in the term of saturation yield, while the parameters most readily controllable, as the current incident on the target and the irradiation time, are expressed.

It is measured, therefore, the produced activity of ^{11}C as a function of irradiation time; normalizing for the saturation activity, it is obtained the graph in fig. 2.6. The ratio between the activity at time t and the saturation activity can be interpreted as the production yield for a given radionuclide at that instant.
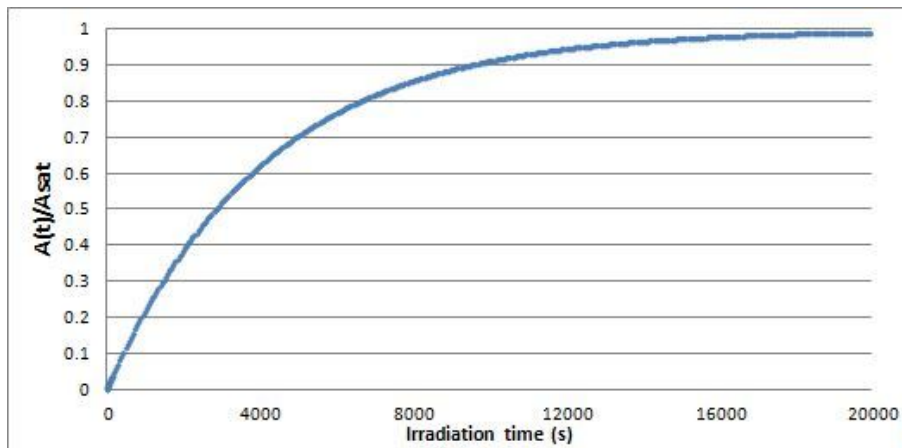

Figure 2.6: Trend of relative activity produced of ^{11}C as a function of irradiation time.

Chapter 3

Monte Carlo simulations

3.1 Introduction

Monte Carlo method is a problem solving technique used to approximate the probability of certain outcomes by running multiple trial runs, called simulations, using random variables. It is named after the city in Monaco, where the primary attractions are casinos that have games of chance: gambling games, like roulette, dice, and slot machines, exhibit random and statistical behavior. They are often used in physical and mathematical problems and are most useful when it is difficult or impossible to obtain a closed-form expression, or unfeasible to apply a deterministic algorithm. Monte Carlo methods are mainly used in three distinct problem classes: optimization, numerical integration and generation of draws from a probability distribution.

In physics-related problems, Monte Carlo methods are quite useful for simulating systems with many coupled degrees of freedom, such as fluids or cellular structures. Other examples include modeling phenomena with significant uncertainty in inputs, such as the calculation of risk in business and, in math, evaluation of multidimensional definite integrals with complicated boundary conditions. This method is widely used in the field of particle and high energy physics, in which is a useful tool for design and optimization of a wide variety of experiments and detection systems. It can be used also in medical physics, such as for X-rays diagnostic, radiotherapy physics, dosimetry, radioprotection, modeling of radiation detectors, and imaging devices in nuclear medicine. This is possible thanks to the increasing availability of ever more powerful computers and supercomputers that are not closely linked to research centers. In

fact, a simulation by means of these techniques, which is implemented for execution by computer, is typically computationally expensive.

The modern version of the Monte Carlo method was invented in the late 1940s by Stanislaw Ulam, while he was working on nuclear weapons projects at the Los Alamos National Laboratory. It was named by Nicholas Metropolis, after the Monte Carlo Casino, where Ulam's uncle often gambled. Immediately after Ulam's breakthrough, John von Neumann understood its importance and programmed the ENIAC computer to carry out Monte Carlo calculations.[13]

Monte Carlo methods vary, but tend to follow a particular pattern:

1. define a domain of possible inputs;

2. generate inputs randomly from a probability distribution over the domain;

3. perform a deterministic computation on the inputs;

4. aggregate the individual results into one final result.

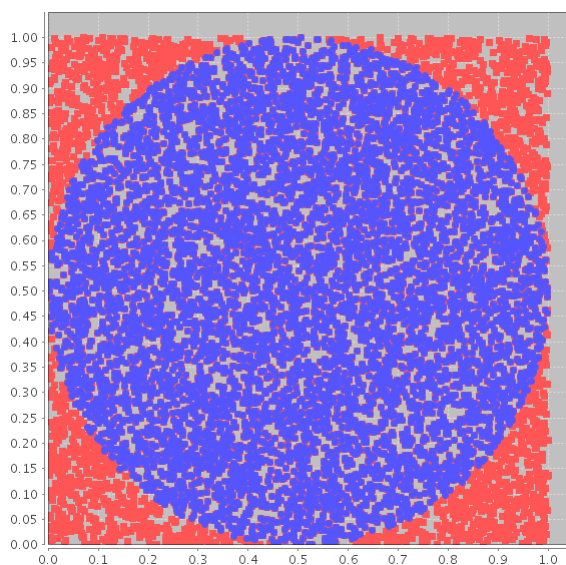The value of π, for example, can be approximated using a Monte Carlo method,

Figure 3.1: Monte Carlo method applied to approximating the value of π.

considering a circle inscribed in a unit square: these have a ratio of areas equal to $\pi/4$. Thus sending random points in the unit square, evaluating the number of points inside the circle and dividing it by the total number of points sent, it is possible to

multiply this number by four to obtain the π value. In this procedure the domain of inputs is the square that circumscribes the circle. Random inputs are generated over the square and then a computation on each input is performed (test whether it falls within the circle). In the end, the results are aggregated to obtain the final result, the approximation of π.[14]

To obtain a simulation with satisfactory results, most of the physical applications of the Monte Carlo method implements the following components:

- PDFs (*probability density functions*) by which the physical system is described;

- generator of random numbers uniformly distributed (usually between 0 and 1);

- sampling rules, i.e. prescriptions for sampling from the specified PDFs;

- methods for estimating the statistical error (*variance*), depending on the number of tests processed;

- variance reduction techniques, in order to reduce the computation time of the simulation;

- management of data and possibility of recording the quantities of interest;

- Parallelization and optimization algorithms for efficient implementation according to available computing architecture.

A fundamental role in Monte Carlo simulations is played by the generation of random numbers using the computer. All generators are based on mathematical algorithms repeatable in itself, for this reason these numbers are called *pseudorandom*. A PRNG (*pseudorandom number generator*) can automatically create long runs of numbers with good random properties, but needs to be initialized by assigning an appropriate value to a numeric parameter or group of parameters, called *seed*, which completely determines the PRNG-generated sequence. One of the most simple PRNG is the *linear congruential generator* (LCG), which is defined by the recurrence relation:

$$X_{n+1} = (a \cdot X_n + c) \bmod m \qquad (3.1)$$

where X is the sequence of pseudorandom values, m (*modulus*) is the maximum number of values that the formula can produce , a and c are two constants, and X_0 is

the seed. If $c = 0$, the generator is often called *multiplicative congruential generator* (MCG).

The characteristics that every generator should have in order to produce a good sequence of pseudorandom numbers, are:

- absent correlation between the numbers in the sequence;

- uniform distribution of the sequence and absence of *bias*;

- high length of the period of the sequence;

- high speed of the algorithm.

From the sequence of numbers uniformly distributed it is necessary to generate random numbers distributed according to the known PDF that describe the process. The following will describe, as example, two methods suitable for the purpose: the *acceptance-rejection* and the *inverse transform* methods.

Rejection sampling is based on the observation that to sample a random variable, one can sample uniformly from the region under the graph of its density function [15, 16].

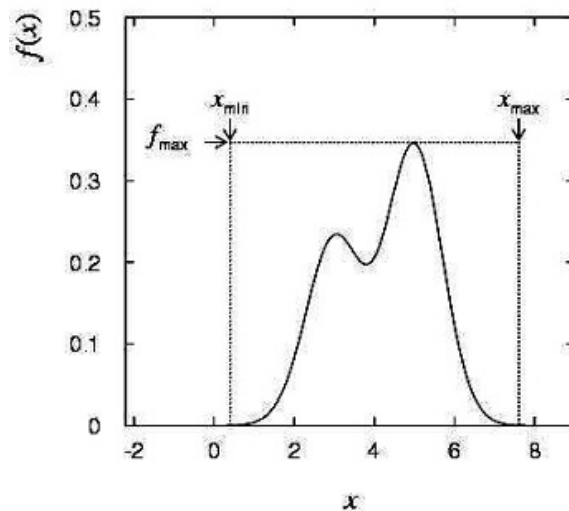Figure 3.2: Rejection method to sample a known PDF.

The rejection method, in its simplest version, is to enclose the PDF of interest $f(x)$ in a rectangle as in the fig. 3.4. Two random numbers, following the uniform distribution between, respectively, x_{min} and x_{max}, and 0 and f_{max}, are extracted. If the second number is less than $f(x)$ it is accepted, otherwise it is rejected and the procedure

is repeated. The general form of rejection sampling assumes that the board is not necessarily rectangular but is shaped according to some distribution that we know how to sample from, and which is at least as high at every point as the distribution we want to sample from, so that the former completely encloses the latter (otherwise, there will be parts of the curved area we want to sample from that can never be reached). Rejection sampling works as follows:

1. sample a point (an x-position) from the proposal distribution;

2. draw a vertical line at this x-position, up to the curve of the proposal distribution;

3. sample uniformly along this line: if the sampled value is greater than the value of the desired distribution at this vertical line, return to step 1.

Since scaling a function by a constant has no effect on the sampled x-positions, this algorithm can be used to sample from a distribution whose probability density function is only known up to a constant, which is common in computational statistics. Although intuitive and applicable to any distribution, this method is rather inefficient because of the numbers discarded.

Inverse transform sampling is a method for generating random numbers from any probability distribution, given its cumulative distribution function (CDF^1) [17]. The *probability integral transform* states that if X is a random variable with a continuous distribution for which the cumulative distribution function is F_X, then the random variable $Y = F_X(X)$ has a uniform distribution between 0 and 1. The inverse transform sampling is just the inverse of this: if Y has a uniform distribution on [0, 1] and if X has a cumulative distribution F_X, then the cumulative distribution function of the random variable $F_X^{-1}(Y)$, if this inverse function exists, is F_X.

Therefore the inverse transform sampling method works as follows:

1. generate a random number r from the standard uniform distribution in the interval [0,1];

2. compute the value x such that $F(x) = r$;

3. take x to be the random number drawn from the distribution described by F.

---

[1]The CDF of a continuous random variable X can be expressed as the integral of its probability density function f_X: $F_X(x) = \int_{-\infty}^{x} f_X(t)\, dt$.
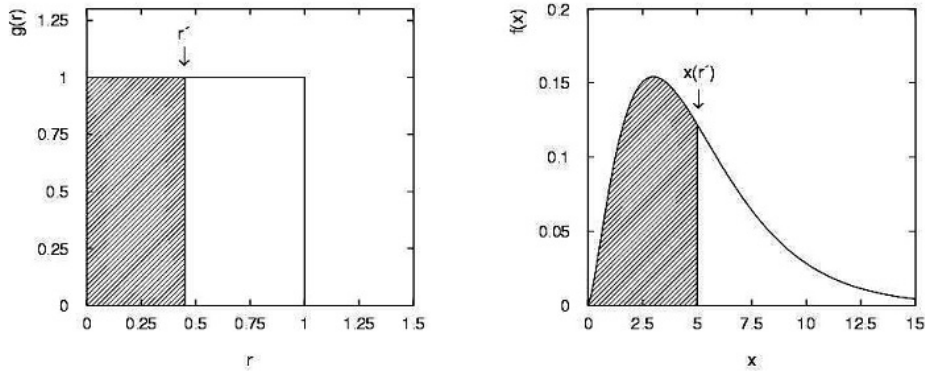
Figure 3.3: Schematic illustration of the inverse transform sampling, which allows to sample a known PDF $f(x)$ from a uniform distribution.

For a Monte Carlo code, it is often necessary to use combinations of these and other methods to be able to generate sequences of numbers following different distributions. Methods of variance reduction are often used, in order to converge more quickly to the result, and thus reduce the time used for the simulation. As seen, in fact, the task of sampling the PDF and further computations necessary for the evolution of the system are assigned to the computer: being the overall calculation of a simulation computationally onerous, optimizations are needed, both at the level of code and in the techniques of simulation.[18, 19, 20]

3.1.1   Monte Carlo platforms currently available for physics application

As mentioned previously, the application of the Monte Carlo method are quite numerous and each field of interest usually has its own implementation of the method adapted and optimized for specific problems. Thus there are numerous software for Monte Carlo simulation, many of which are specially designed for specific physical applications.

In high-energy physics specific *event generators*, i.e. software libraries that generate simulated high-energy particle physics events, are used [25, 26]. Examples are PYTHIA[27], which simulates collisions of high-energy particle, and CompHEP[28], witch is a software package for automatic computations in high-energy physics of collision events or particle decays.

General purpose software for Monte Carlo simulations are: *EGS4, MCNP, Pene-*

lope, *FLUKA* and *Geant4*.

The *Electron Gamma Shower* (EGS4)[29] computer code system is a general purpose package for Monte Carlo simulation of the coupled transport of electrons and photons in an arbitrary geometry; it was originally developed at SLAC for the high-energy (TeV), and now the field of application has been extended to lower energies (few keV), thanks to projects such as EGSnrc and BEAMnrc. The EGSnrc[30] system is a package for the Monte Carlo simulation of coupled electron-photon transport; its energy range of applicability is considered to be 1 keV÷10 GeV and it is particularly well-suited for medical physics purposes, such as the research and development of devices that allow medical professionals to detect radiation, represent a patient's anatomy using X-rays, or deliver a prescribed radiation dose to a tumor while sparing healthy tissue. The software is also employed directly by medical physicists in cancer clinics for research and for verifying radiation treatment plans. BEAMnrc[31] allows to simulate beams of electrons and photons travelling through consecutive material components, ranging from simple slabs to complex collimators. BEAMnrc is built around the core EGSnrc and its main application is to model the treatment planning of radiotherapy linear particle accelerators (LINACs) used by medical physicists to treat cancer. Due to its flexible, modular design and companion utilities, this software can also be used for a vast range of applications, including the simulation of research and industrial LINAC beams, X-ray emitters, radiation dose delivery to a patient, radiation shielding, and more.

MCNP[32] is a general-purpose Monte Carlo code with which it is possible to simulate the physics of neutrons and that can be used for neutron, photon, and electron or coupled neutron/photon/electron transport. It includes methods of variance reduction and is used in a wide range of applications: from medical physics, radiation protection and dosimetry, to the design of detectors and the design of nuclear reactors.

PENELOPE[33] performs Monte Carlo simulation of coupled electron-photon transport in arbitrary materials for a wide energy range, from a few hundred eV to about 1 GeV, sufficient for the physical processes involved in a PET scan. A mixed procedure is used for the simulation of electron and positron interactions, in which "hard" events are simulated in a detailed way, while "soft" interactions are calculated from multiple scattering approaches.

FLUKA[34, 35] is a general purpose Monte Carlo tool for calculations of particle trans-

port and interactions with matter, covering an extended range of applications spanning from proton and electron accelerator shielding to target design, calorimetry, activation, dosimetry, detector design, Accelerator Driven Systems, cosmic rays, neutrino physics, radiotherapy etc. FLUKA can simulate with high accuracy the interaction and propagation in matter of about 60 different particles, including photons and electrons from 1 keV to thousands of TeV, neutrinos, muons of any energy, hadrons of energies up to 20 TeV (up to 10 PeV by linking FLUKA with the DPMJET code) and all the corresponding antiparticles, neutrons down to thermal energies and heavy ions. The program can also transport polarized photons (e.g., synchrotron radiation) and optical photons. Time evolution and tracking of emitted radiation from unstable residual nuclei can be performed online. A graphical user interface to run FLUKA named *Flair* has been developed using *Python* and is available at the project website.

Geant4[36, 37], which will be discussed in more detail in one of the next sections, is a toolkit for the simulation of the passage of particles through matter. It is the successor of the GEANT series of software toolkits developed at CERN, and the first to use object oriented programming (in C++). Geant4 package was originally designed for high energy physics experiments, but has found applications also outside this domain in the areas of medical and biological sciences, radiation protection and astronautics.

3.1.2   Monte Carlo simulations in Nuclear Medicine

There has been an enormous increase of interest in the use of Monte Carlo techniques in all aspects of nuclear imaging instrumentation design and quantification, including SPECT (*Single Photon Emission Computed Tomography*), PET and multi-modality imaging devices, due to the intrinsically probabilistic nature of the processes of emission, transport and detection of the radiation.[21, 22, 23]

Assuming that the behavior of the imaging system can be described by PDFs, then the Monte Carlo simulation can proceed by sampling from these PDFs, which necessitates a fast way to generate uniformly distributed random numbers. The simulation of a nuclear medical imaging system with Monte Carlo techniques consists of:

1. the simulation of the particles emitted by the radioactive sources distributed inside the patient;

2. the time evolution of their tracks, determined by the initial conditions and by

the interactions with the system modeled and with detectors;

3. the collection of information about events.

Simulation codes could contain a database of cross sections, which express the interaction probability of the particles with the medium through which they are transported. These data could also be derived by means of specific physical models, using a database of quantity experimentally or theoretically obtained. Each cross section is typical of the physical process involved, energy and materials used in the simulated geometry, and through them the specific PDFs are sampled from random numbers uniformly distributed. The history of a particle is terminated according to specific conditions, such as the exit from the volume of interest or the achievement of a certain energy threshold. The outcomes of this random sampling must be accumulated in an appropriate manner to produce the desired result and in order to reach a solution of the physical problem.
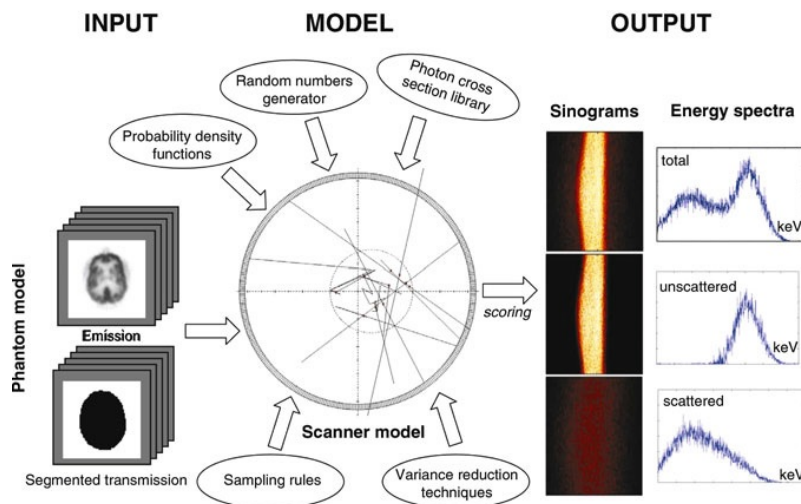

Figure 3.4: Principles and main components of a Monte Carlo program dedicated to simulation of cylindrical multi-ring PET imaging systems.[24]

The applications of the Monte Carlo method in nuclear medical imaging cover almost all topics, including detector modelling and systems design, image correction and reconstruction techniques, dosimetry, radioprotection and pharmacokinetic modelling.

3.2   Geant4

Geant4 is a open source software toolkit, written in C++, for simulating the passage of particles through matter, using Monte Carlo methods. It covers a complete range of functionality and, in defining and implementing the software components, all aspects of the simulation process have been included: the geometry of the system, the materials involved, the generation and production of particles of interest, the tracking of particles through materials and external electromagnetic fields, the physics processes governing particle interactions, the response of sensitive detector components, the generation of event data, the storage of events and tracks, the visualization of the detector and particle trajectories, and the capture for subsequent analysis of simulation data at different levels of detail and refinement.

The available physics processes a comprehensive range, including electromagnetic, hadronic and optical processes, a large set of long-lived particles, materials and elements, over a wide energy range.

The toolkit—designed and developed by an international collaboration formed by individuals from a number of cooperating institutes, HEP (*High Energy Physics*) experiments, and universities—has been created exploiting software engineering and object-oriented technology and implemented in the *C++* programming language. It has been used in applications in particle physics, nuclear physics, accelerator design, space engineering and medical physics.

The origin of Geant4 development (the name is an acronym formed from "GEometry ANd Tracking") can be traced back to two studies done independently at *CERN* and *KEK* in 1993. Both groups sought to investigate how modern computing techniques could be applied to improve what was offered by the existing *GEANT3* program (written in *FORTRAN* and dating back to 1974), which was a benchmark and source of ideas and valuable experience. These two activities merged and a proposal was submitted to the CERN *Detector Research and Development Committee* (DRDC) to construct a simulation program based on object-oriented technology. The resulting project was *RD44*, a worldwide collaboration that grew to include the efforts of 100 scientists and engineers, drawn from more than 10 experiments in Europe, Russia, Japan, Canada and the United States. The R&D phase was completed in December 1998 with the delivery of the first production release.

Subsequently the Geant4 Collaboration was established in January 1999 to con-

tinue the development and refinement of the toolkit, and to provide maintenance and support. The Collaboration provides documentation, that includes installation, user guides and a range of training kits, and user support, that covers help with problems relating to the code, consultation on using the toolkit and responding to enhancement requests.

3.2.1 General considerations

Geant4, just as any general purpose Monte Carlo software system, contains components (event generator, detector simulation, reconstruction and analysis) that can be used separately or in combinations, thus it has well-defined interfaces between different components. Moreover it is modular and flexible, and its implementation of physics is transparent and open to validation: it should allow the user to customize and extend it in all domains. Its modular architecture should enable the user to pick only those components he/she needs.

The high-level design was based on an analysis of the initial user requirements: this has led to a modular and hierarchical structure for the toolkit (see fig. 3.5), where subdomains are linked by a uni-directional flow of dependencies. The key domains of the simulation of the passage of particles through matter are:

- geometry and materials;

- particle interaction in matter;

- tracking management;

- digitization and hit management;

- event and track management;

- visualization and visualization framework;

- user interface.

These domains are defined by class categories with coherent interfaces and, for each category, there is a corresponding working group with a well defined responsibility.

Geant4 takes advantage of advanced software engineering techniques to deliver these key requirements of functionality, modularity, extensibility and openness.

The toolkit offers the user the ability to create a geometrical model with a large number of components of different shapes and materials, and to record information about physical quantities of interest. Geant4 provides a comprehensive set of physics processes to model the behavior of particles. The user can choose from different approaches and implementations, and to modify or add to the set provided. Furthermore it is possible to interact with the toolkit through a set of (graphical) interfaces and visualize the geometry and tracks with a variety of graphics systems through a well-defined interface and is given the ability to implement this interface on other systems.

In general, the classes in the toolkit are designed in a highly reusable and a compact way so that users can extend or modify their services for specific applications.It is possible to realize this by following the discipline of object-oriented technology.

Object oriented technology allows to establish a clear and customizable correspondence between particles and processes and offer different models for each process. The choice between the provided models is fast and relatively simple, but what is not easy is to customize the physical models, in order to make them more suitable for the reactions of interest.

The cross sections are calculated via formulas, parameterizations or interpolation of databases. In the last case the information extracted from the database is separated from the way it is accessed and used, giving the opportunity of using different databases and allowing their applicability to be tailored by particle, energy, material, etc. Similarly the generation of the final state is separated from the calculation of the cross sections used for tracking and is also split into alternative or complementary models, according to the energy, range, particle type and material.

3.2.2 Global structure

For this thesis work it was used the 10.0 release of Geant4, the latest available.

The design has evolved during development and is still evolving. Fig. 3.5 shows the top level categories and illustrates how each category depends on the others. There is a uni-directional flow of dependencies, i.e. no circular dependencies, as required.

Categories at the bottom of the diagram are virtually used by all higher categories and provide the basic framework of the toolkit.
These categories include:

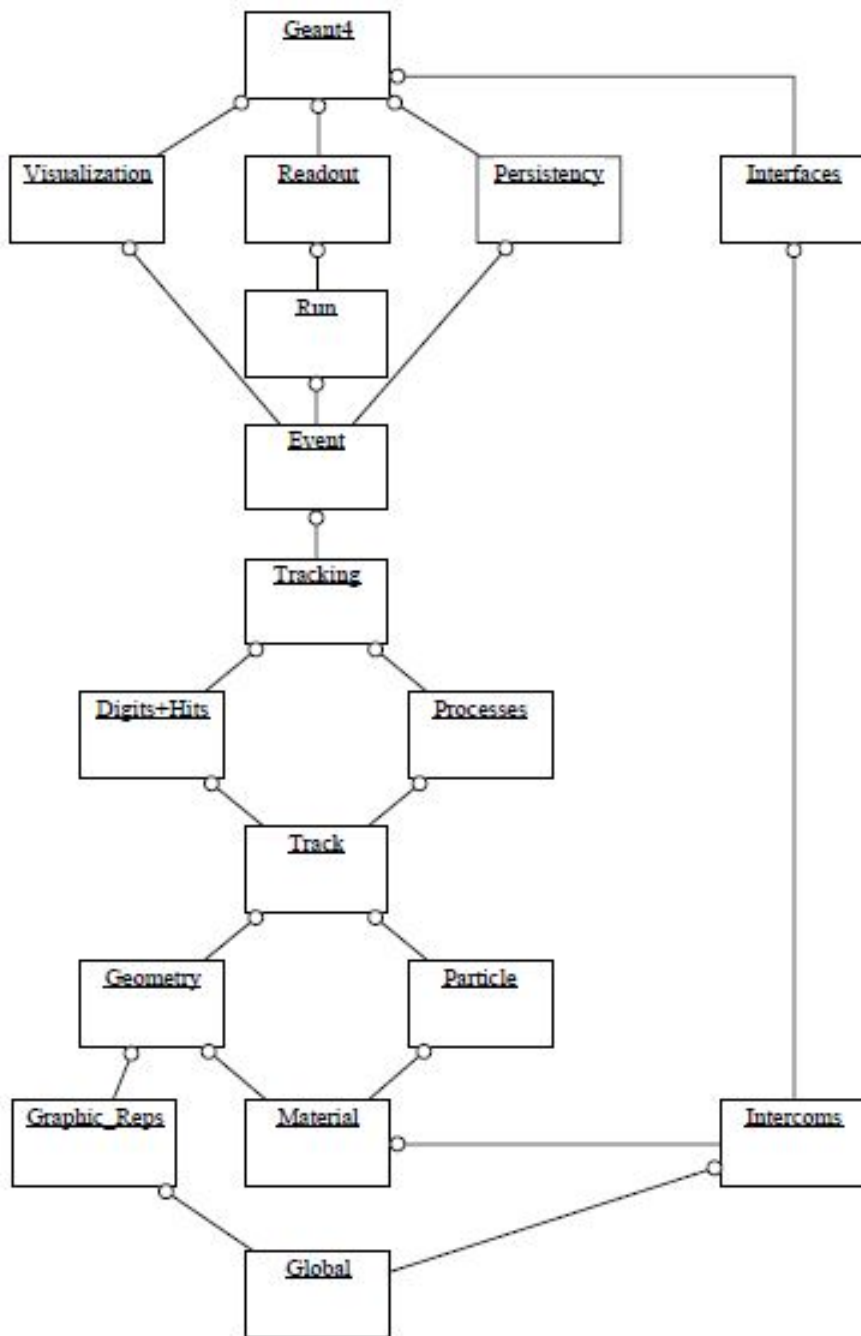- the category *global* covering the system of units, constants, numerics and random

Figure 3.5: The Top Level Category Diagram of the Geant4 toolkit. The open circle on the joining lines represents a using relationship; the category at the circle end uses the adjoined category.

number handling;

- *graphical representations*;

- *materials*;

- *particles*;

- *geometry* including the volumes for detector description and the navigation in the geometry model;

- *intercoms* which provides both a means of interacting with Geant4 through the user interface and also a way of communicating between modules that should not otherwise depend on one another. Intercoms is also the repository of abstract interfaces for *plugins.*

Over these, there are the categories required to describe the tracking of particles and the physical processes. The *track* category contains classes for tracks and steps, used by *processes* which contains implementations of models of physical interactions. Additionally, *transportation* process, handles the transport of particles in the geometry model and, optionally, allows the triggering of parameterizations of processes. All these processes may be invoked by the *tracking* category, which manages their contribution to the evolution of a track state and it has the task to provide information in sensitive volumes for hits and digitization.

Over these, the *event* category manages events in terms of their tracks and *run* manages collections of events that share a common beam and detector implementation. A *readout* category allows the handling of output data of interest.

Finally, *visualization*, *persistency* and *interface* categories allow the use of all the mentioned categories, providing (abstract) interfaces with the toolkit.

3.2.3 Simulations with Geant4

In order to create a simulation with Geant4, it is necessary to write a program using C++ language. Within the *main* function, the *G4RunManager* class manages the whole simulation and it allow to register eight user classes [38]. The concrete implementation, initialization and registration of these classes are mandatory in three cases, optional in the other five instances. This enables the user to customize Geant4 for specific needs.

The three mandatory user class bases are:

- *G4VUserDetectorConstruction* for defining the material and geometrical setup of the detector. Several other properties, such as detector sensitivities and visualization attributes, are also defined in this class;

- *G4VUserPhysicsList* for defining all the particles, physics processes and cut-off parameters;

- *G4VUserPrimaryGeneratorAction* for generating the primary vertices and particles.

For these three user classes, Geant4 provides no default behavior; instead there are pure abstract definitions from which the user must derive her/his own concrete classes. For example, Geant4 defines no default physics process. Because of this, the user can easily switch any specific physics process without affecting any other processes.

The optional user classes allow the user to modify the default behavior of Geant4. The five optional user classes are:

- *G4UserRunAction* for actions at the beginning and end of every run;

- *G4UserEventAction* for actions at the beginning and end of every event;

- *G4UserStackingAction* for customizing access to the track stacks;

- *G4UserTrackingAction* for actions at the creation and completion of every track;

- *G4UserSteppingAction* for customizing behavior at every step.

Simulation architecture

The three mandatory classes provide the foundation necessary for the simulation of a given physical system.

The *G4VUserDetectorConstruction* abstract class and its derived classes (*concrete classes*) allows to define both materials and the whole geometrical setup of the model of interest. Some concepts about the description of geometrical structures have been borrowed from previous simulation packages, but improvements, refinements and advances have been made in some key areas.

The concepts of *logical* and *physical volume* are not unlike those of GEANT3. A logical volume (*G4LogicalVolume*) represents a detector element of a certain shape that can hold other volumes inside it and can have other attributes; it also has access to other information that is independent of its physical position in the detector, such as material. A physical volume (*G4PhysicalVolume*) represents the spatial positioning of the logical volume with respect to an enclosing mother (logical) volume. Thus a

hierarchical tree structure of volumes can be built, each volume containing smaller volumes.

In Geant4 the logical volume has been refined by defining the shape as a separate entity, named *solid*. Solids with simple shapes, like rectilinear boxes (*G4Box*), trapezoids (*G4Trd*), spherical and cylindrical sections (*G4Sphere* and *G4Tubs*), have their properties coded separately, in agreement with the concept of *Constructive Solid Geometry* (CSG). More complex solids are defined by their bounding surfaces and belong to the *Boundary Representations* (BREPs) sub-category. Another way of obtaining solids is by boolean operations (union, intersection, subtraction and their compositions).

The classes (*G4Material, G4Element, G4Isotope*) are related to materials used for the construction of the geometrical structures and they reflect what exists in nature: materials are made of a single element or a mixture of elements, and elements are made of a single isotope or a mixture of isotopes. Because the physical properties of materials can be described in a generic way by quantities which can be either given directly, like density, or derived from the element composition, only concrete classes are provided in this category.

G4VUserPhysicsList is an abstract class for constructing particles and processes.

Particles are based on the *G4ParticleDefinition* class, which describes the basic properties, like mass and charge, and also allows the particle to carry the list of processes to which it is sensitive. A first-level extension of this class defines the interface for particles that carry cuts information, for example range-cut versus energy-cut equivalence. A set of virtual intermediate classes allows the implementation of concrete particle classes, such as *G4Electron* or *G4PionMinus*, which define the particle properties and, in particular, implement the actual range versus energy cuts equivalence.

Physics processes describe how particles interact with materials. Geant4 provides seven major categories of processes:

- electromagnetic;

- hadronic;

- decay;

- optical;

- photolepton-hadron;

- trasportation;

- parameterization.

G4VProcess is the base class for all physics processes. Each physics process must implement virtual methods of G4VProcess which describe the interaction (*DoIt* methods) and determine when an interaction should occur (*GetPhysicalInteractionLength* methods).

There are several methods to define a Physics List starting with G4VUserPhysicsList virtual class.

- A possibility is to derive a concrete class from G4VUserPhysicsList and implement three virtual methods:

- *ConstructParticle()* to instantiate each requested particle type;

- *ConstructProcess()* to instantiate the desired physics processes and register each of them;

- *SetCuts(G4double aValue)* to set a cut value in range for all particles in the particle table, which invokes the rebuilding of the physics table.

The ConstructProcess() method must always invoke the *AddTransportation()* method in order to ensure particle transportation.

- A number of ready-to-use Physics Lists, implementing a defined setup, are available with Geant4 kernel. The full set of reference Physics Lists is described in the Geant4 documentation.

- The user Physics List class may be created from components provided by Geant4 kernel and by user application. For that *G4VModularPhysicsList*, a derived class of G4VUserPhysicsList, should be implemented. It is not mandatory to record all types of physical processes, then only the interactions of interest can be considered.

In *SetCuts*, a method of the G4VUserPhysicsList virtual class, the threshold value for secondary particle production should be defined as a distance, which is internally converted to an energy for each material.

The *G4VUserPrimaryGeneratorAction* class allows to specify how primary particles are generated. Actual generation of primary particles will be done by concrete classes

of G4VPrimaryGenerator, such as *G4ParticleGun* and *G4GeneralParticleSource.* G4-ParticleGun class generates primary particle(s) with a given momentum and position. G4GeneralParticleSource, a more advanced primary generator, allows the specifications of the spectral, spatial and angular distribution of the primary source particles.

Run and track

In Geant4, *run* consists of a sequence of events and is the largest unit of a simulation. Within a run, the detector geometry, the set up of sensitive detectors, and the physics processes used in the simulation are kept unchanged. It is represented by a *G4Run* class and starts with *BeamOn()* method of *G4RunManager.* G4Run has a run identification number, which should be set by the user, and the number of events simulated during the run.

G4Event class represents an event, which is the main unit of simulation. An object of this class contains all inputs and, optionally, outputs of the simulated event. It contains primary vertices and primary particles before processing the event. After processing, it has hits and digitizations generated by the simulation and, optionally, trajectories of the simulated particles. The fact that G4Event is independent of other classes also benefits pile-up simulation. Digitization can be postponed until the processing of two or more events on a rolling basis and G4Event objects can be "added" to each other.

G4Track class represents a track, that is a snapshot of a particle within its environment. When the production of secondary particles occurs, G4Track objects are consequently created. G4Track keeps "current" information of the particle (i.e. energy, momentum, position and time) and has "static" information (i.e. mass and charge) also. As the particle moves, the quantities in the snapshot are updated. For optimization reasons, the physical quantities before the update are discarded by default. It is up to the user to record the quantities of interest, as will be described in the next section. Secondary particles are transported as separate tracks, therefore in case of secondaries production new G4Track objects are suitably created. Track object is deleted when:

- it leaves the *world* volume;

- it disappears (particle decays or is absorbed);

- it goes down to zero kinetic energy and no *at rest* process is defined;

- the user decides to delete it artificially.

G4Step class represents a step, which provides information about a process occurred. It includes the two endpoints, *PreStepPoint* and *PostStepPoint*, and also stores the change in track properties between the two points. These properties, such as energy and momentum, are updated as the various active processes are invoked. If step is limited by a boundary, the end point stands exactly on the boundary, but it logically belongs to the next volume.
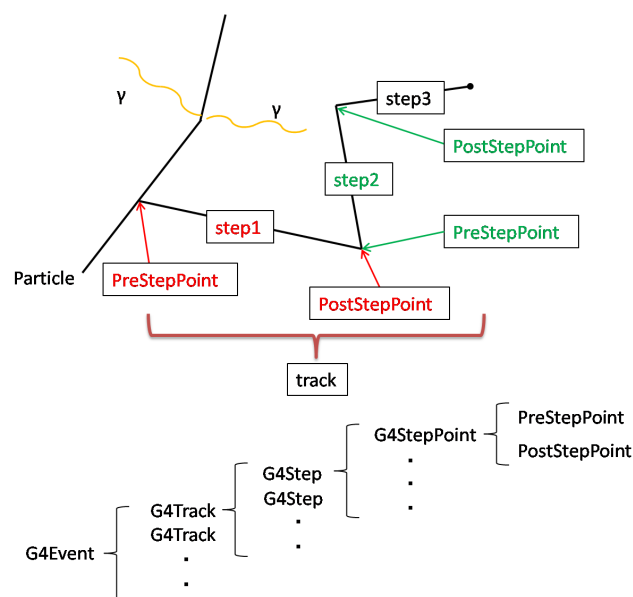

Figure 3.6: Schematic representation of an event with its tracks. Each track (only one is completely represented) contains several steps, each of which shows the pre-step and the post-step points.

Scoring and visualization

G4VSensitiveDetector is an abstract base class which represents a detector, thanks to which useful information from the simulation could be extracted. The principal mandate of a detector is the construction of hit objects (snapshots of the physical interaction of a track in the sensitive region of a detector), using information from steps along a particle track. *G4MultiFunctionalDetector* is a concrete class derived from G4VSensitiveDetector. Instead of implementing a user-specific detector class, G4MultiFunctionalDetector allows the user to register *G4VPrimitiveScorer* classes in order to extract physical quantities from a specific volume. G4MultiFunctionalDetector

should be instantiated in the users detector construction with its unique name and should be assigned to one or more G4LogicalVolumes.

Geant4 allows the graphical view of the simulated system and the tracks generated by the particles, with different options of visualization available. The *G4VisManager* class must be initialized, and the options can also be changed from a input file by means of a simple macro language.

The user can also define a scoring mesh through the *G4ScoringBox* or the *G4ScoringCylinder* classes, setting size, position, rotation and binning for the mesh. There is an arbitrary number of quantities to be scored for each cell of the mesh, optionally setting filters. Scored data can be graphically visualized, drawing slices or projections, and is also possible to dump scores in a mesh to a file.
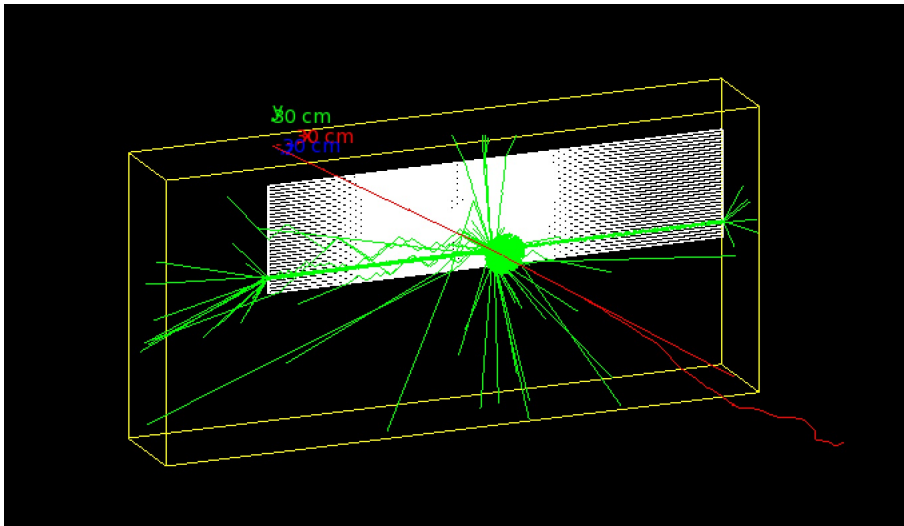
Figure 3.7: Representation of a simulated system with Geant4. Particle tracks can be seen colored according to their charge.

Chapter 4

Simulation of ^{11}C target

In this chapter the modeling with Geant4 of the PETTrace ^{11}C target will be discussed in detail. Moreover, scoring and output analysis with the ROOT toolkit will be described.

4.1 Target model

For this Monte Carlo simulation, the PETTrace components subsequent to the *beam extraction system*, where the electrons of negative hydrogen ions are removed, leaving only protons, were modeled. The interest, indeed, is related to the components that may affect the ^{11}C production and the target itself.

For the simulated geometry, as it can be seen in fig. 4.3, simple shapes like rectangular boxes (*G4Box*), cylindrical sections (*G4Tubs*) and cylindrical cut sections (*G4CutTubs*) were used. The geometry was built using the *Construct* function of *myC11TargetDetectorConstruction*, the concrete class suitably derived from *G4VUserDetectorConstruction* virtual class.

The main parent volume (*world*), consists of a cube of air, whose sides measure 120 cm. Inside was placed the modeled structure, that can be divided into three main parts:

1. proton collimator;

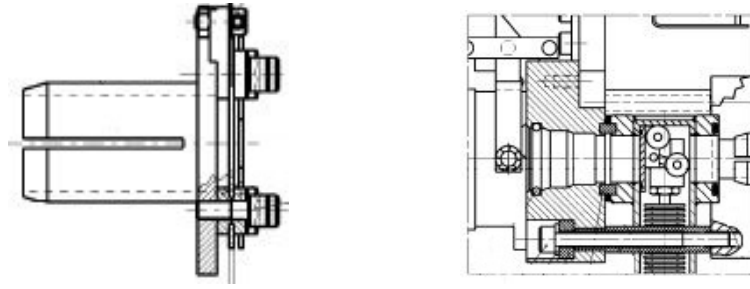2. *Beam Exit Valve* (BEV);

3. ^{11}C target.

Figure 4.1: On the left, it is shown a collimator section. On the right, it can be seen a BEV representation.[6]

Before the collimator, a cylindrical *beamline* of 1 cm radius and 10 cm long, containing high vacuum (defined as hydrogen gas with a density of 10^{-24} g/cm^3), was placed. The beamline simulates the distance crossed by the protons just accelerated, before passing through the collimator.

1) The collimator is composed of:

- a graphite box with base area of 3.8×7.4 cm^2 and 1 cm thick, with a central hole 1.0×0.8 cm^2. This is the proper collimator.

- an aluminum cylinder of 2.6 cm radius, 0.4 cm thick, with a cylindrical central hole of 0.75 cm radius.

- an aluminum cylinder of 1.3 cm radius, 0.4 cm thick, with a cylindrical central hole of 0.75 cm radius.

2) The BEV was modeled much simpler than the real one: the purpose was in fact to reproduce the passage of protons inside it, and not to simulate all the mechanical connection of the target to the structure of cyclotron. The BEV was composed of an aluminum box with base area of 5.6×5.6 cm^2 and 0.6 cm long, which is linked to the cyclotron structure, and an aluminum cylinder of 1.65 cm radius and 4.8 cm thick. Both structures have a central hole, respectively of 0.75 cm and 0.85 cm radius.

3) ^{11}C target was divided into 4 sub-structures: a front flange, the helium cooling flange, the proper high-pressure nitrogen target, and the rear flange. In order to simulate the inexact alignment of the ^{11}C target, the model is suitably designed to make it possible to change its orientation with respect to the fixed parts (collimator and BEV).
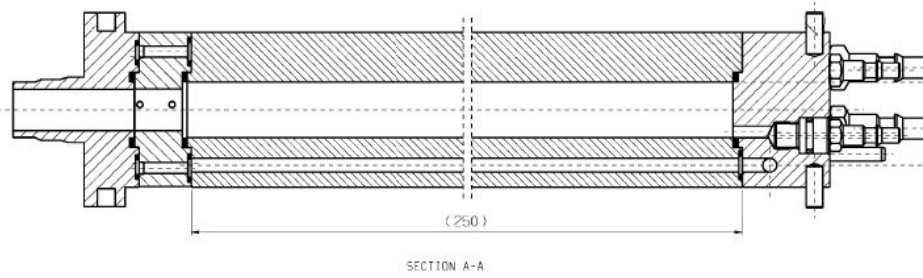
Figure 4.2: Section of ^{11}C target.[6]

The front flange is composed of an aluminum cylinder of 1.125 cm radius, and an aluminum box with a base area of 5.6×5.6 cm^2 and 1.9 cm thick, both with a central hole of 0.75 cm radius.

The helium cooling flange is formed of an Havar^{TM} cubic foil with 2.7 cm side and 25 μm thick, an aluminum box with base area of 5.6×5.6 cm^2 and 1.9 cm thick, and another Havar^{TM} cubic foil that is 50 μm thick. The aluminum box has a central hole of 0.75 cm radius, which is filled with high-pressure helium (601325 Pa).

The high-pressure nitrogen chamber is composed of an aluminum box with base area of 5.6×5.6 cm^2 and 25 cm thick. This box has a central hole of 0.975 cm radius, which is filled with high-pressure (1.342375 MPa $\cong$ 194.695 psi) mixture of molecular nitrogen (99%) and molecular oxygen (1%).
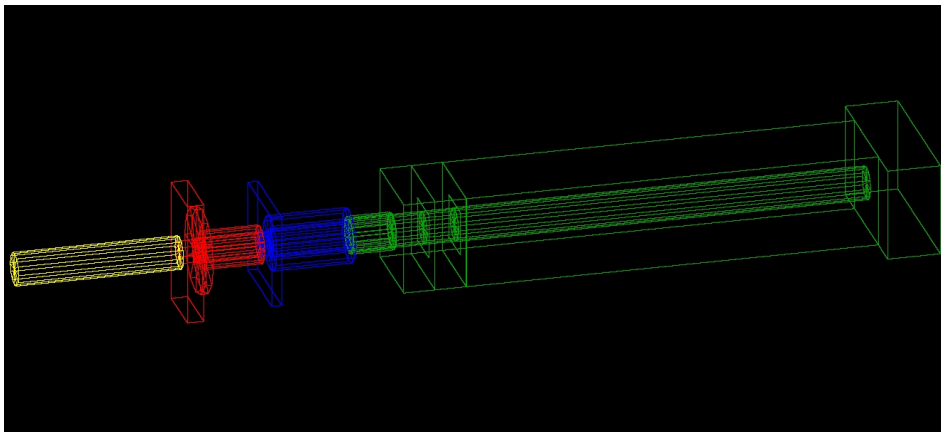

Figure 4.3: Simulated geometry. Beamline is represented in yellow, collimator in red, BEV in blue and the ^{11}C target with the rear flange in green.

Finally, the rear flange is an aluminum box with base area of 10×5.6 cm^2 and 3.2 cm thick.

In an initial set of simulations, aimed to find the optimal parameters of the Physics List to be used, comparing reached results with validated data, a simplified geometry was utilized. The use of a simplified model allows, indeed, to obtain results that depend only on the selected Physics List component and it also reduces the computation time significantly.

The simplified structure, as it can be seen in fig. 4.4, was composed of a cylindrical beamline of 1 cm radius and 6.5 cm long, containing high vacuum (defined as hydrogen gas with a density of 10^{-24} g/cm^3), a high-pressure nitrogen chamber, and a rear flange. The nitrogen chamber is composed of an aluminum box with base area of 5.6×5.6 cm^2 and 25 cm thick. This box has a central hole of 0.975 cm radius, which is filled with high-pressure (1.342375 MPa $\cong$ 194.695 psi) molecular nitrogen (99%). The rear flange is an aluminum box with base area of 10×5.6 cm^2 and 3.2 cm thick.
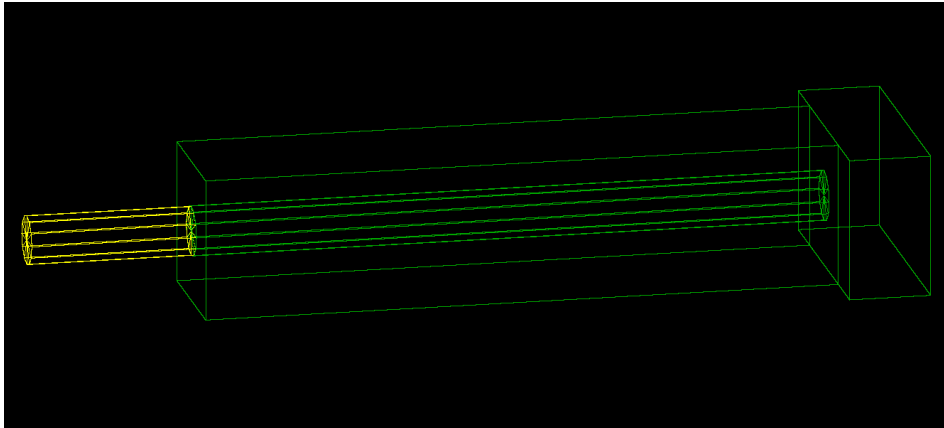

Figure 4.4: Simulated simplified geometry. Beamline is represented in yellow and the ^{11}C target with the rear frange in green.

4.2 Source model

The particle source, placed at the beginning of the beamline, shoots a proton for each simulated event and, according to the requirement, the number of primary protons was modified each time. The source is modeled in the *myC11TargetPrimaryGeneratorAction* class, derived from *G4VUserPrimaryGeneratorAction*, using *G4ParticleGun* class.

In the *GeneratePrimaries* function, kinetic energy, initial position and direction of the protons were selected. In order to simulate gaussian distributions, mean and

standard deviation must be provided to the function *shoot* of the class *RandGauss*, which is part of *CLHEP* class libraries, which are integrated within Geant4.

Each proton was generated with a kinetic energy of 16.5±0.1 MeV (k=3), that is gaussian distributed, based on the factory data.

The source is not point-like, but, in the directions perpendicular to the trajectory of the beam, it is gaussian distributed around zero (σ_x=0.28 cm and σ_y=0.25 cm). These spatial distributions were evaluated from *paper burn*s (burns caused by the proton beam that passes through a paper, which represent the transverse sections of the beam) at the entry position of ^{11}C target and at the end position of the nitrogen chamber, and experimental data about the beam current registered on the collimator and the current which reaches the target ($\frac{I_{collimator}}{I_{target}} \approx 22\%$).

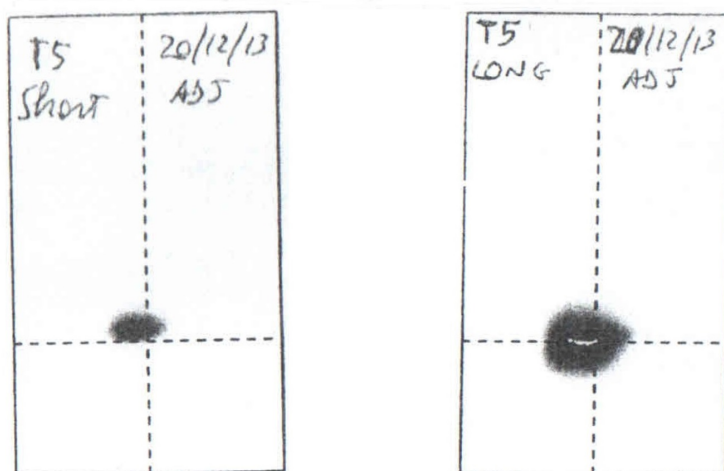Figure 4.5: Paper burns for the ^{11}C target. On the left there is the paper burn taken at the entry position of the ^{11}C target, on the right the paper burn taken at the end position of the nitrogen chamber.

Finally a small gaussian angular dispersion in the directions perpendicular to the trajectory of the primary protons was assumed (momenta p_x=p_y=(0±0.0036)·p_{tot}, with k=1), in order to simulate the inexact alignment of the protons in the beam.

4.3   Physics List

In *myC11TargetPhysicsList*, a class derived from *G4VModularPhysicsList* virtual class, the physics processes to take into account were added and selected. In *SetCuts* method,

the range-cuts (threshold values of secondary production) were set as default (1 mm) for all particles.

Registering the *G4DecayPhysics* class in the Physics List, all particles of interest, such as protons, electrons, positrons, gamma particles, neutrons, unstable nuclei, and their weak decays were defined.

G4EmStandardPhysics, standard class of Geant4 for electromagnetism, was used in order to define the electromagnetic processes, which constitute the majority of the physical processes that occur to primary protons while interacting within the target material. The non-use of classes which take advantage of more detailed approximation models and lower energy cuts, also improves computational time.

In order to validate some results, SRIM[39], a collection of software packages that allow the calculation of many parameters regarding the transport of ions in matter, the results of which are validated by various research centers[40], was used.

It was considered sufficient to use the standard electromagnetic physics since, evaluating the energy of primary protons at the entry of the nitrogen chamber, values compatible with SRIM data were obtained, as it can be seen in the next chapter. Moreover, evaluating the proton mean range at the energies of interest in the high-pressure nitrogen chamber with G4EmStandardPhysics, it was obtained a value comparable to the result provided by *G4EmPenelopePhysics*, a class which uses Penelope models (models with great care to low energy description[41]). Using G4EmPenelopePhysics the simulations are also 25% slower.

G4HadronElasticPhysics class was registered in order to define the elastic processes between hadrons: this is the standard class for this type of processes and it is normally used in the various examples provided by Geant4.

For hadron inelastic interactions an in-depth analysis was performed, in order to properly simulate processes of nuclear activation that occur in the target. Geant4, in fact, has been developed for high energy physics and, while many validation works at low energies were performed for the electromagnetic interactions, the results for the hadronic processes, available in the literature, are few and not always satisfactory.

First, it was utilized the *QBBC* class, which provides a ready-to-use Physics List. QBBC Physics List utilizes *Binary Cascade* model[42] to describes hadronic processes. As it can be seen in the next chapter, the ^{11}C saturation yield measured using Binary Cascade model for primary protons at the energies of interest, was greater than that

expected.

It was, therefore, tried to build a Physics List class from components provided by Geant4 kernel. Performing several tests, it was seen that the best hadronic components of the Physics List are those which use Binary Cascade model or *Precompound* model[43]. In fig. 4.6 are shown the recommended hadronic models, according to the involved energies: classes suggested are the two mentioned and *Bertini Intranuclear Cascade* model[45], which in testing did not give satisfactory results.
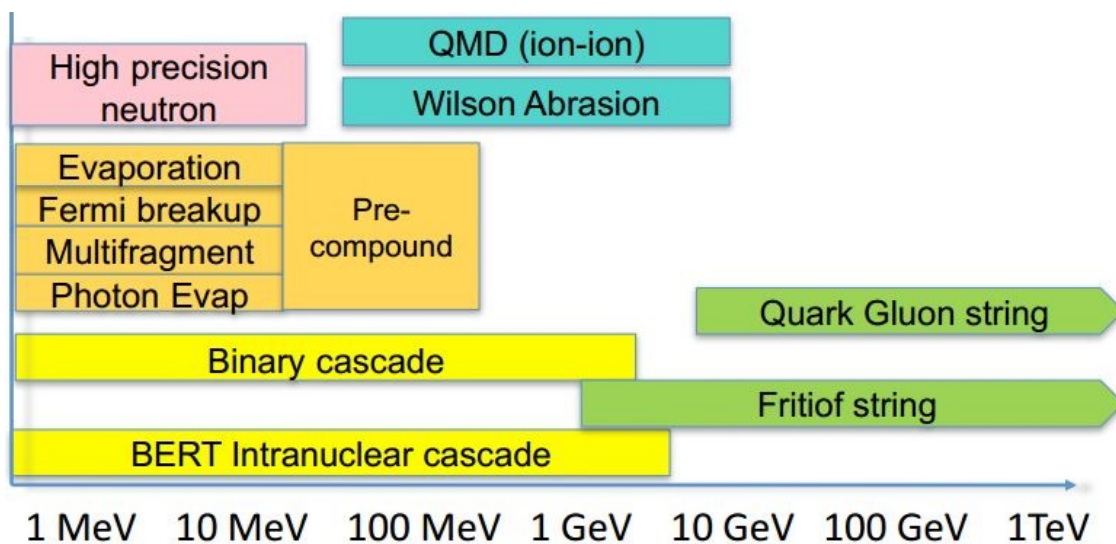

Figure 4.6: List of recommended hadron inelastic model, as function of energy[44].

Then a new hadron inelastic physics class was written and registered in the Physics List, modifying the existing *G4HadronPhysicsQGSP_BIC* class. In order to choose proton cross sections, *INCLXXProtonBuilder* class was also customized. The Geant4 inelastic cross section expresses the total probability of inelastic processes for a specific incident particle, and not the probabilities for each channel of interaction, such as (p,α) reactions, which are calculated from the approximation model (i.e. Binary, Precompound, Bertini, etc.), using inelastic cross section and information about materials.

The best results for the ^{11}C saturation yield, as it can be seen in the next chapter, were provided by Precompound model, using *G4ChipsProtonInelasticXS* or *G4IonProtonCrossSection* cross section classes, and Binary model.

4.4   Output analysis

Setting one or more volumes in the function *ConstructDandField* of myC11Target-DetectorConstruction class as multifunctional detector, the target components were selected as sensitive detectors. Suitably implementing the *Initialize*, *ProcessHits* and *EndOfEvent* functions of myC11TargetTrackerSD class, derived from G4MultiFunctionalDetector class, we can get the data of interest.

Information about the type and position of physics processes, which occur in the sensitive region for each generated primary protons, were extracted from the *PostStep-Point*s of the current steps (*G4Step*). From the position vector, the projection (*posZ*) along the straight line passing through the center and parallel to the lateral side of the nitrogen chamber, the distance from this line (*radius*), and the azimuthal angle (*phi*) on a plane perpendicular to this line and passing through the point in which the process occur, were taken. The angle is counterclockwise measured with respect to the vector on the plane that connects the point in which the process occur with the straight line.

Also the residual kinetic energy of the primary particles was extracted from the PostStepPoints.

The primary particle names and IDs, which represent the primary identification numbers, were taken from the track state (*G4Track*) concerning the current step. Information about secondary particles and the deposited energy were directly extracted through the current step.

Filtering all the processes, except the hadron inelastic processes, such as *protonInelastic* and *neutronInelastic*, a *for* loop was implemented in order to record, for each step, the secondary particle names, their kinetic energy, the emission angle with respect to the momentum direction of the primary particle and, from the *PreStepPoint*, the production energy of the secondary particles. For optimization reason secondary electrons and gamma particles were not recorded for this specific process.

Two different sensitive regions were created in order to evaluate the number of primary protons incident on the collimator and the target. The proton current was estimated by counting each primary proton (track identification number or TrackID=1) that enters in the region (first step of each event).

The kinetic energy of the primary protons at the entry of the high-pressure nitrogen chamber was evaluated from the first PreStepPoint of each event.

The mean range of primary protons in the high-pressure nitrogen chamber was estimated selecting the posZ for the last PostStepPoint of each event.

Since we were able to count the number of isotopes that were produced during the irradiation, the ^{11}C saturation yield was evaluated by dividing the number of the produced ^{11}C nuclei by the number of primary protons that enter into the high-pressure nitrogen chamber. These values, expressed in produced nuclei for incident protons, were subsequently converted in mCi/μA, an unit of measure widely used in radionuclide production.

These results, with the exception of the proton current, were analyzed with *ROOT*. ROOT[46] is an object-oriented program and library developed by CERN. The ROOT system provides a set of frameworks with all the functionality needed to store, handle and analyze large amounts of data in a very efficient way.

The ROOT developers had designed the *TTree* class in order to store large quantities of same-class objects. These objects are stored in files optimized to reduce disk usage and enhance access speed. A TTree is a list of *TBranch*es, each of which contain the variables of interest, that are called leaf (*TLeaf*). The leafs are organized in the branches according to the type of the variable.

In our Geant4/C++ program three TTree were created and stored in a single output file. Each TTree was filled with the quantities of interest at run-time, event by event, through proper code implemented within the myC11TargetTrackerSD previously described. Primary kinetic energy, deposited energy, primary names, type of interactions and interaction positions (posZ, radius and phi) were stored in the first TTree. In the second TTree the secondary names for hadron inelastic processes were stored along with their kinetic energy, the emission angles, the production energies, the production positions, and the primary names. Finally, the kinetic energy of the primary protons at the entry of the high-pressure nitrogen chamber was stored in the third TTree.

The TTree object allows to create histograms with the data of interest, to combine these data in multidimensional histograms, and to filters a variable type according to other information which it contains. In the histograms it is possible to select the number of the bins, their size and the interval of interest.

We had set various filters directly by ROOT, in order to select, for example, the primary particles of a specific type of process or the kinetic energy of particles of interest. In fig. 4.7 it can be seen, for example, the type of process which occur when

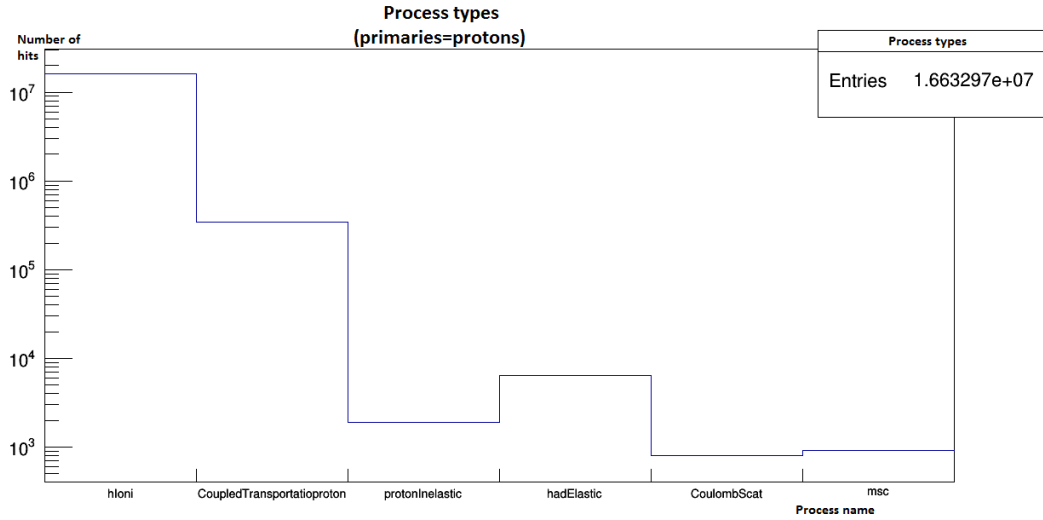the primary particles are protons, and in fig. 4.8 it is shown the secondary kinetic energy generated by *protonInelastic* processes.

Figure 4.7: Type of processes which occur in ^{11}C target when the primary particles are protons. The graph is reached by shooting 1E6 protons and plotting the results with ROOT.
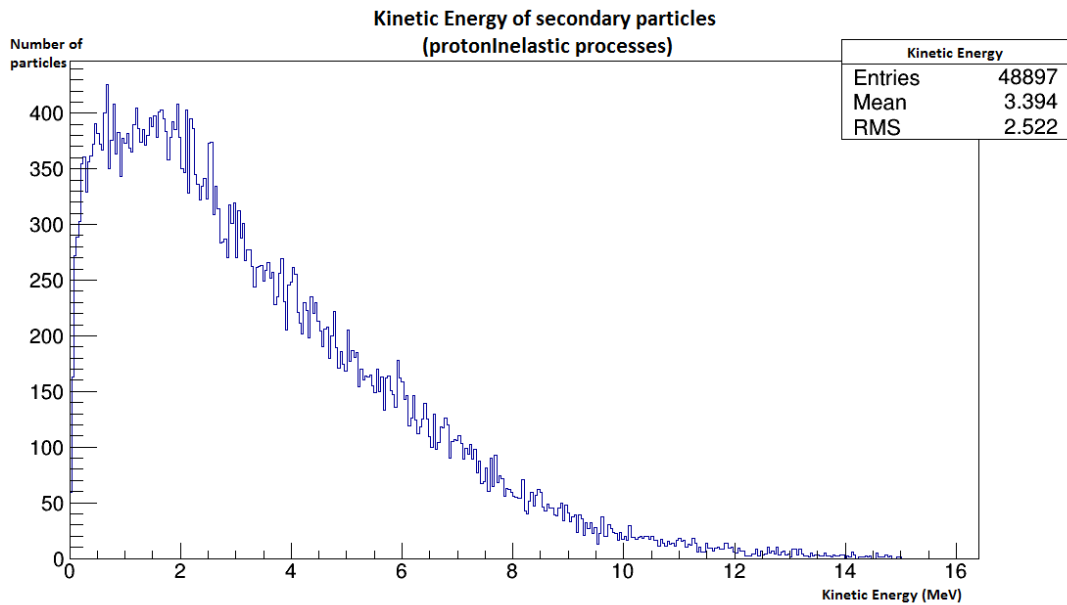

Figure 4.8: Kinetic energy of secondary particles when they are produced by protonInelastic processes. The graph is reached by shooting 1E7 protons and plotting the results with ROOT.

Scoring of deposited energy of absorbed dose was also carried out through the *OpenGL* graphical interface of Geant4, which allows the visualization in 3-D of the simulated environment both in real time or after a run. The data about material slices or projections were drawn and filtered according to particle type, their electric charge or kinetic energy. Scoring meshes were defined, positioned and drawn using macro commands provided through an input file prior to the initialization of the simulation. The volumes were drawn in the same file, representing just the contours, in order to see what happens inside them.

Finally, particle tracks were visualized together with the simulated geometry, as it can be seen in fig 4.9. The colors are different according to particle type, and hits were drawn at end of each event. All events in a run were superimposed and it is possible to make video, drawing tracks by time, in order to get a visual idea of what happens inside the target. This is also a helpful tool for a preliminary, qualitative check of the simulation setup. Even in this case, the tracks were drawn, with the volumes, using macro commands in *vis.mac* file.
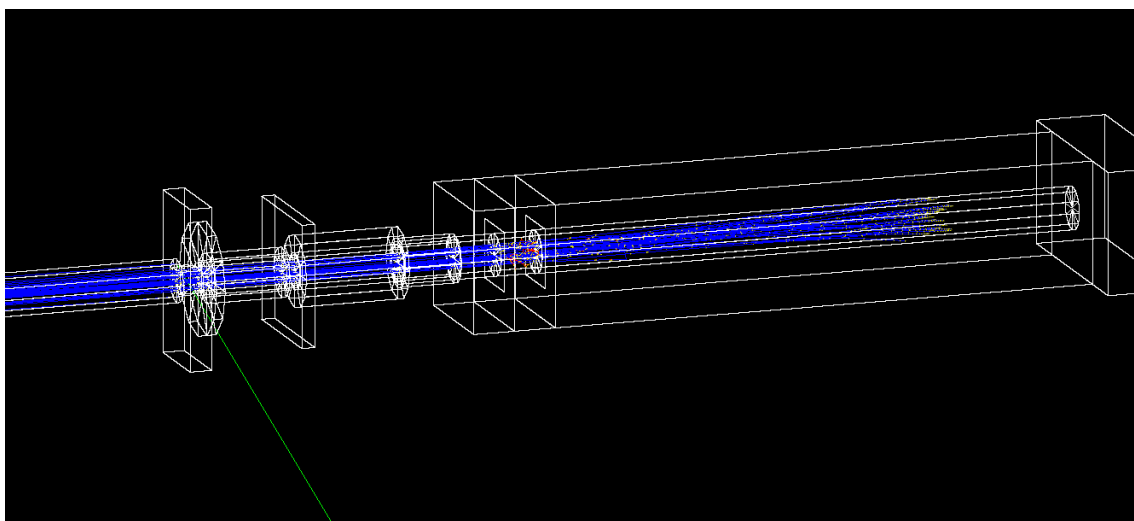

Figure 4.9: Graphic view of the tracks in the simulated geometry. Protons are drawn in blue, electrons in red and gamma particles in green. In yellow are marked hit positions. 50 protons are sent during the run.

Chapter 5

Results

5.1 Entry kinetic energy and proton range

Using Geant4, the kinetic energy of primary protons at the entry of the high-pressure nitrogen chamber was evaluated (the protons have passed the two Havar^{TM} foils and the high-pressure helium chamber). As it can be seen from fig. 5.1, obtained by plotting the Geant4 results in a histogram with ROOT, the average kinetic energy (1E6 protons shot) is equal to 15.22±0.01 MeV, compatible, within the errors, with SRIM value of 15.22±0.01 MeV, obtained by shooting 1E4 protons.
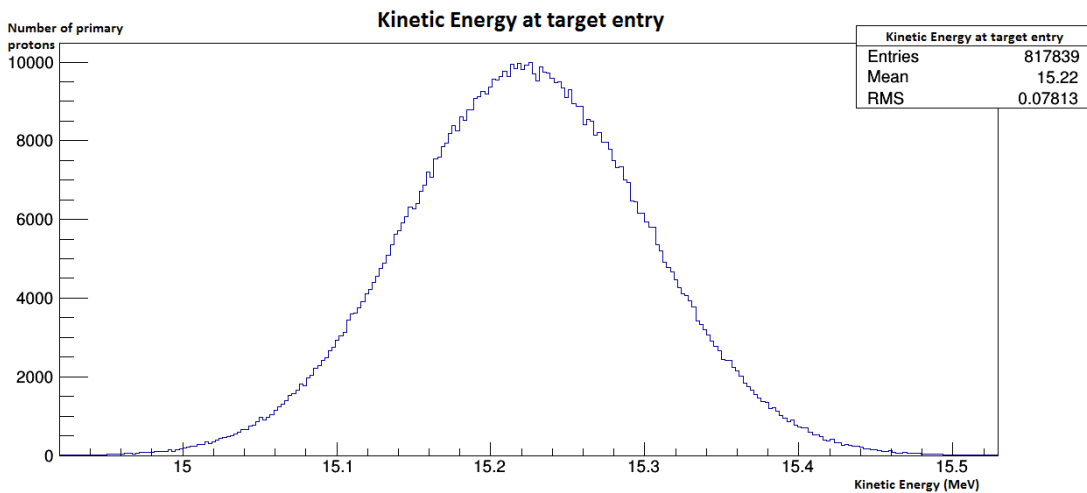
Figure 5.1: Kinetic Energy of primary protons at the entrance of the high-pressure nitrogen chamber. The graph was reached by shooting 1E6 protons and plotting the results with ROOT.

Therefore, as it can be seen in fig. 5.2 and 5.3, we estimated the mean range of 15.22 MeV protons (point-like beam) in the high-pressure nitrogen chamber (sim-

plified target), shooting 1E6 protons, both with the standard electromagnetic class (G4EMStandardPhysics) and G4EMPenelopePhysics class. The standard class provided a value of 18.82±0.01 cm, while, using the Penelope models, it was obtained 18.79±0.01 cm. Comparing the first result with SRIM value (19.05±0.01 cm, by shooting 1E4 protons), it was underlined a relative difference of about 1.2%. The Penelope models, instead, provided a lower value and, therefore, a higher relative difference with respect to SRIM.
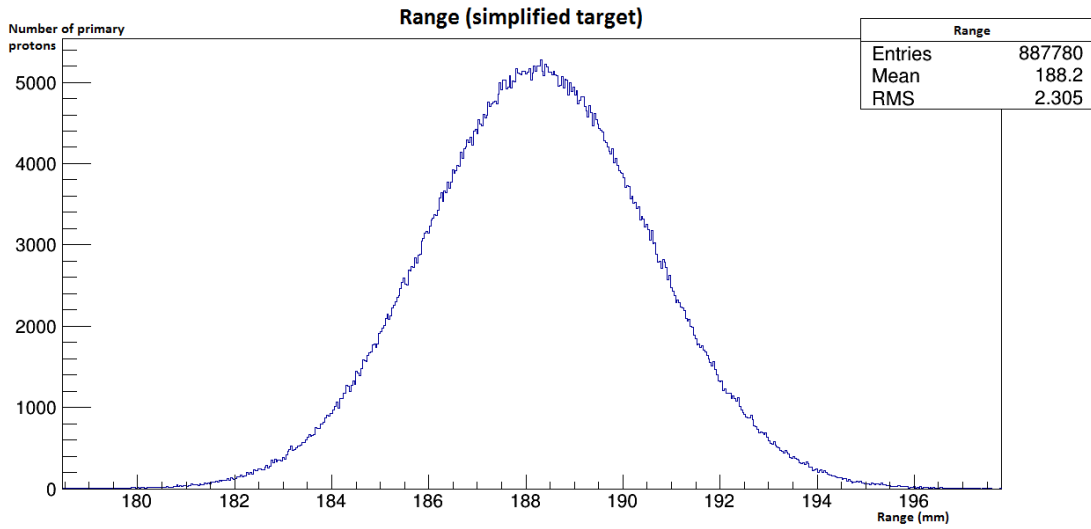
Figure 5.2: Protons range in the simplified target. The graph was reached by shooting 1E6 protons and plotting the results with ROOT.

SRIM mean range in the high-pressure nitrogen for 16.5 MeV protons, which passed through the two Havar^{TM} foils and the high-pressure helium chamber, was of 19.05±0.01 cm (obtained by shooting 1E4 protons). As it can be seen from the fig. 5.4, Geant4 provided, shooting 1E6 protons, a mean range of 18.83±0.01 cm. Their relative difference is about 1.2%. This number must be interpreted considering that SRIM does not allow to set an energy spread, in contrast with Geant4 simulations (E_0=16.5±0.1 MeV, with k=3). Furthermore, the proton beam simulated in Geant4 had a small angular dispersion, that affected the longitudinal range, while the SRIM simulation did not take this into account this.
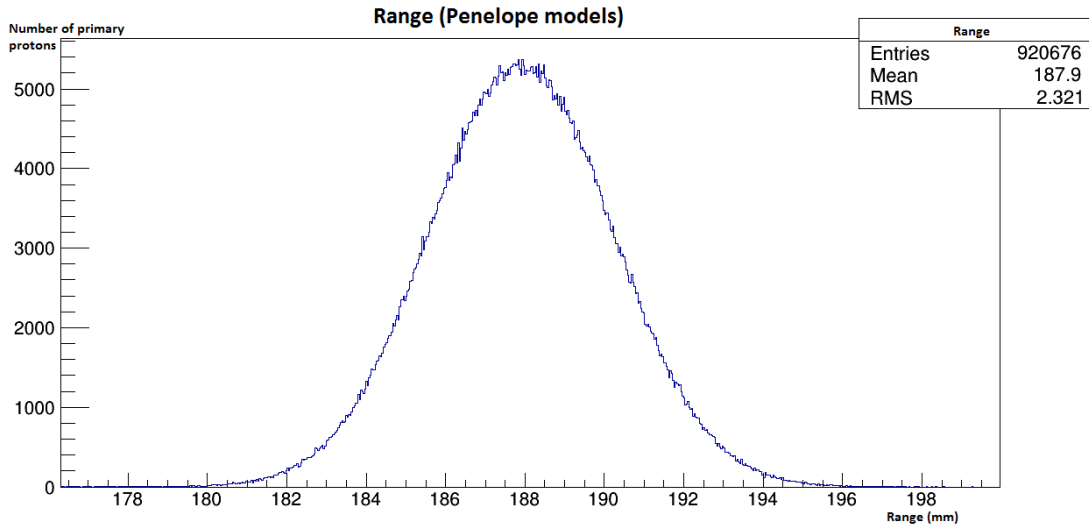
Figure 5.3: Protons range in the simplified target using the G4EMPenelopePhysics class. The graph was reached by shooting 1E6 protons and plotting the results with ROOT.
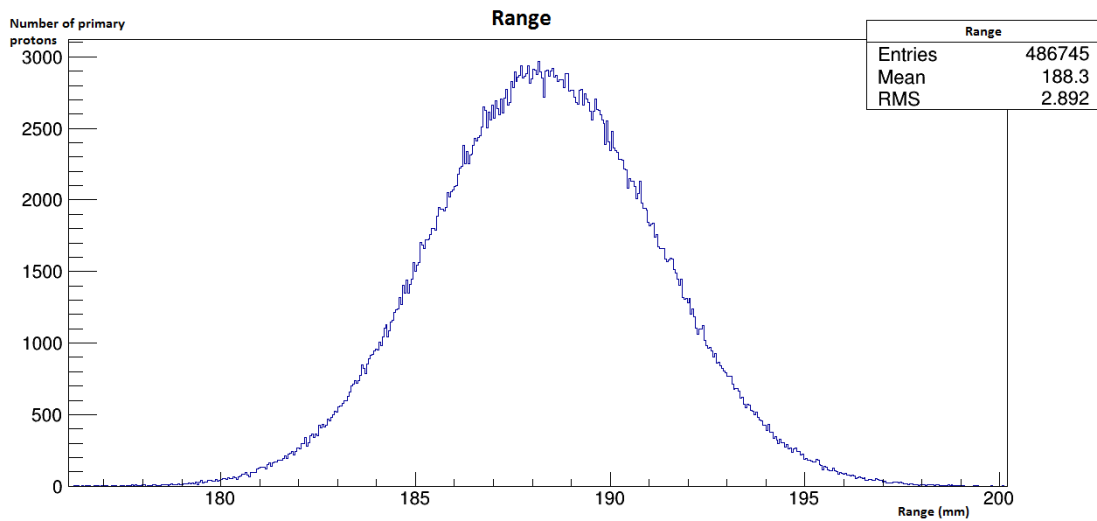

Figure 5.4: Protons range in the modeled target. The graph was reached by shooting 1E6 protons and plotting the results with ROOT.

Figure 5.5 shows all the energy deposited by 1E7 protons in the high-pressure nitrogen. The values were projected on the inner lateral side of the nitrogen chamber. As it can be seen, a peak of deposited energy (Bragg Peak) occurred immediately before that the particles come to rest.

Moreover, the position of the Bragg peak was estimated both with Geant4 (18.60±0.05 cm) and SRIM (18.80±0.13 cm) in order to compare the results. Their relative difference is about 1.1%, however, the values are compatible within the sampling errors.
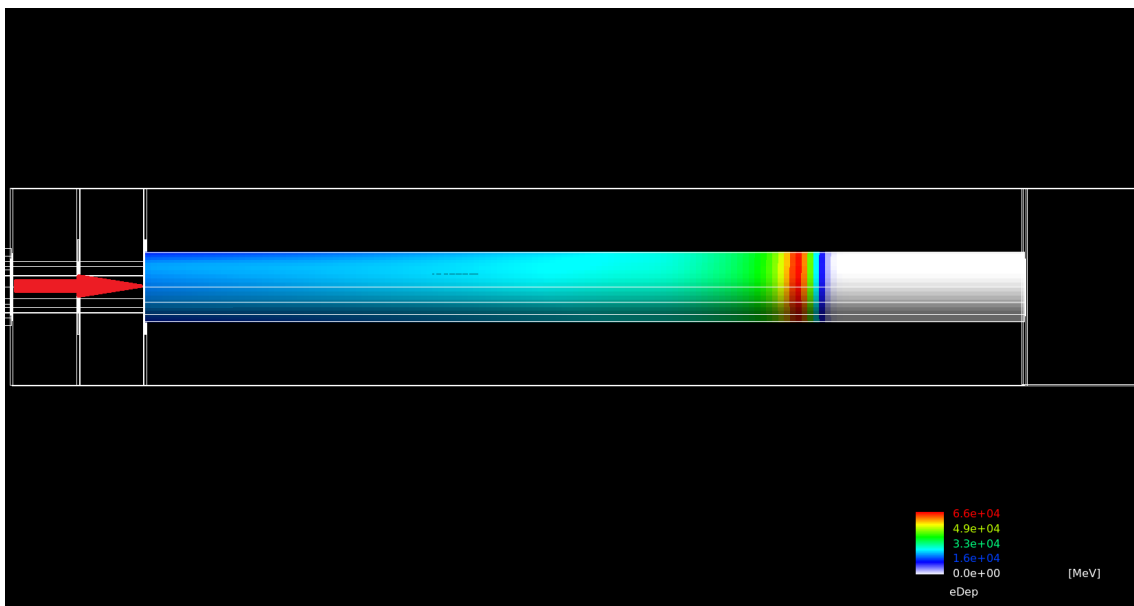

Figure 5.5: Scoring mesh of the energy deposited in the nitrogen by 1E7 protons. The mesh was superimposed on the target geometry. The red arrow specifies the direction of the proton beam.

5.2 Saturation yield

5.2.1 ^{11}C saturation yield as a function of energy

To evaluate the adequacy of the physics classes adopted, it was measured the ^{11}C saturation yield as a function of energy, using the simplified target and shooting 1E6 protons each time. The table 5.1 shows the measured values for the physics models that were tested. In the figures 5.6, 5.7, 5.8 these data versus those of IAEA were plotted, and in fig. 5.9 the average of this values versus IAEA data was reported.

Energy (MeV)	ChipsInelXS Y_{sat} (mCi/μA)	IonProtonXS Y_{sat} (mCi/μA)	Binary Y_{sat} (mCi/μA)	Average Y_{sat} (mCi/μA)	IAEA Y_{sat} (mCi/μA)
5.7	0.0 ± 0.0	0.0 ± 0.0	0.0 ± 0.0	0.0 ± 0.0	3.0 ± 0.3
6.0	0.3 ± 0.2	0.8 ± 0.4	0.5 ± 0.3	0.6 ± 0.3	5.1 ± 0.5
6.3	1.2 ± 0.4	3.0 ± 0.7	1.3 ± 0.5	1.9 ± 0.9	6.7 ± 0.7
6.6	1.3 ± 0.5	5.9 ± 1.0	2.0 ± 0.6	3.1 ± 1.8	10.1 ± 1.0
6.9	3.5 ± 0.8	8.4 ± 1.2	4.2 ± 0.8	5.4 ± 2.1	16.9 ± 1.7
7.2	3.0 ± 0.7	13.0 ± 1.5	7.8 ± 1.1	8 ± 4	21.9 ± 2.2
7.5	4.6 ± 0.9	17.0 ± 1.7	12.6 ± 1.5	11 ± 4	32 ± 3
7.8	8.9 ± 1.2	19.6 ± 1.8	14.8 ± 1.6	14 ± 4	42 ± 4
8.1	10.0 ± 1.3	20.7 ± 1.9	17.4 ± 1.7	16 ± 4	49 ± 5
8.4	10.3 ± 1.3	31.0 ± 2.3	23.4 ± 2.0	22 ± 7	52 ± 5
8.7	12.1 ± 1.4	30.4 ± 2.3	23.4 ± 2.0	22 ± 6	56 ± 6
9.0	16.2 ± 1.7	37.1 ± 2.5	29.9 ± 2.2	28 ± 7	59 ± 6
9.3	20.7 ± 1.9	40.5 ± 2.6	31.0 ± 2.3	31 ± 7	62 ± 6
9.6	22.4 ± 1.9	43.0 ± 2.7	38.5 ± 2.5	35 ± 8	68 ± 7
9.9	23.8 ± 2.0	47.2 ± 2.8	40.5 ± 2.6	37 ± 8	71 ± 7
10.2	27.7 ± 2.2	50.6 ± 2.9	47.2 ± 2.8	42 ± 9	74 ± 7
10.5	35.2 ± 2.4	54 ± 3	50.6 ± 2.9	47 ± 7	81 ± 8
10.8	35.8 ± 2.5	62 ± 3	50.6 ± 2.9	50 ± 9	86 ± 9
11.1	37.6 ± 2.5	71 ± 3	64 ± 3	58 ± 12	91 ± 9
11.4	42.2 ± 2.7	69 ± 3	74 ± 4	62 ± 12	98 ± 10
11.7	48.9 ± 2.9	73 ± 3	81 ± 4	67 ± 12	103 ± 10
12.0	57 ± 3	88 ± 4	96 ± 4	80 ± 14	108 ± 11
12.3	64 ± 3	86 ± 4	101 ± 4	84 ± 13	113 ± 11
12.6	67 ± 3	100 ± 4	116 ± 4	94 ± 17	120 ± 12
12.9	79 ± 4	108 ± 4	123 ± 5	103 ± 15	127 ± 13
13.2	93 ± 4	120 ± 4	137 ± 5	116 ± 15	133 ± 13
13.5	103 ± 4	125 ± 5	147 ± 5	125 ± 15	140 ± 14
13.8	118 ± 4	140 ± 5	169 ± 5	142 ± 17	148 ± 15
14.1	128 ± 5	153 ± 5	174 ± 5	152 ± 16	157 ± 16

Energy	ChipsInelXS	IonProtonXS	Binary	Average	IAEA
(MeV)	Y_{sat} (mCi/μA)	Y_{sat} (mCi/μA)	Y_{sat} (mCi/μA)	Y_{sat} (mCi/μA)	Y_{sat} (mCi/μA)
14.4	140 ± 5	159 ± 5	199 ± 6	166 ± 20	164 ± 16
14.7	143 ± 5	167 ± 5	202 ± 6	171 ± 20	169 ± 17
15.0	159 ± 5	191 ± 6	228 ± 6	192 ± 23	175 ± 18
15.2	177 ± 5	192 ± 6	228 ± 6	199 ± 19	180 ± 18
15.3	182 ± 6	201 ± 6	245 ± 6	209 ± 22	182 ± 18
15.6	201 ± 6	214 ± 6	250 ± 6	221 ± 18	189 ± 19
15.9	216 ± 6	238 ± 6	253 ± 7	236 ± 14	196 ± 20
16.2	233 ± 6	248 ± 6	290 ± 7	257 ± 21	202 ± 20
16.5	241 ± 6	265 ± 7	307 ± 7	271 ± 23	209 ± 21

Table 5.1: ^{11}C saturation yield at different energies, changing type of hadron inelastic model (Precompound with G4ChipsProtonInelasticXS, Precompound with G4IonProtonCrossSection, and Binary), and average value of these data. The last column shows IAEA data (error=10%), useful for comparison[2, 47]. The values were measured shooting 1E6 protons and errors, which are propagation of uncertainties related to the Poisson distribution, were added to measures. The error associated to the average values is the sum of propagated uncertainty (assuming independent errors), and SDOM (standard deviation of the mean).
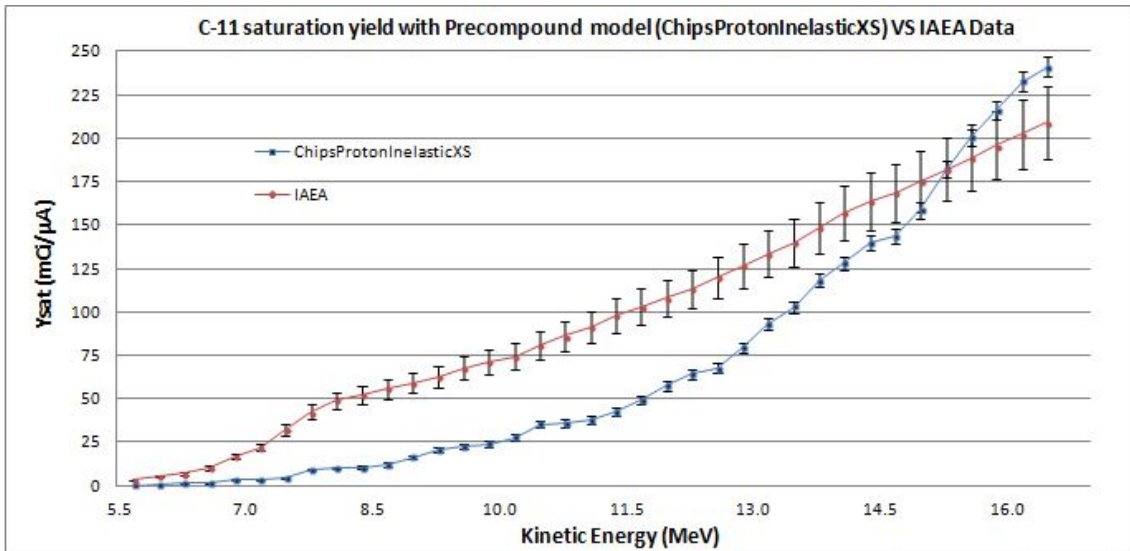

Figure 5.6: Comparison between ^{11}C saturation yield as a function of energy, using Precompound model with G4ChipsProtonInelasticXS cross section class, and IAEA data.

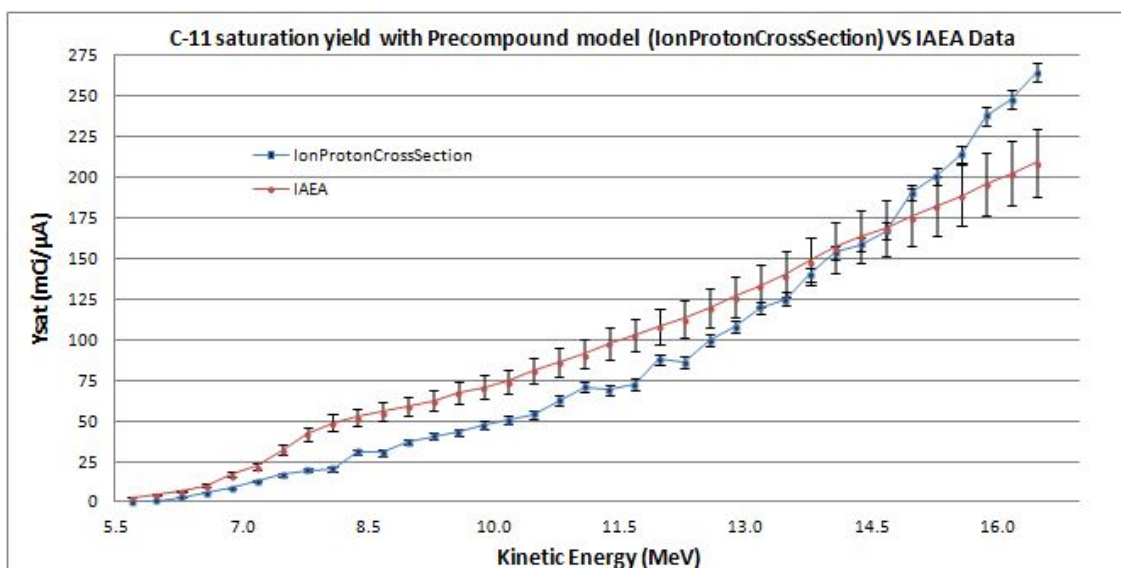Figure 5.7: Comparison between ^{11}C saturation yield as a function of energy, using Precompound model with G4IonProtonCrossSection cross section class, and IAEA data.

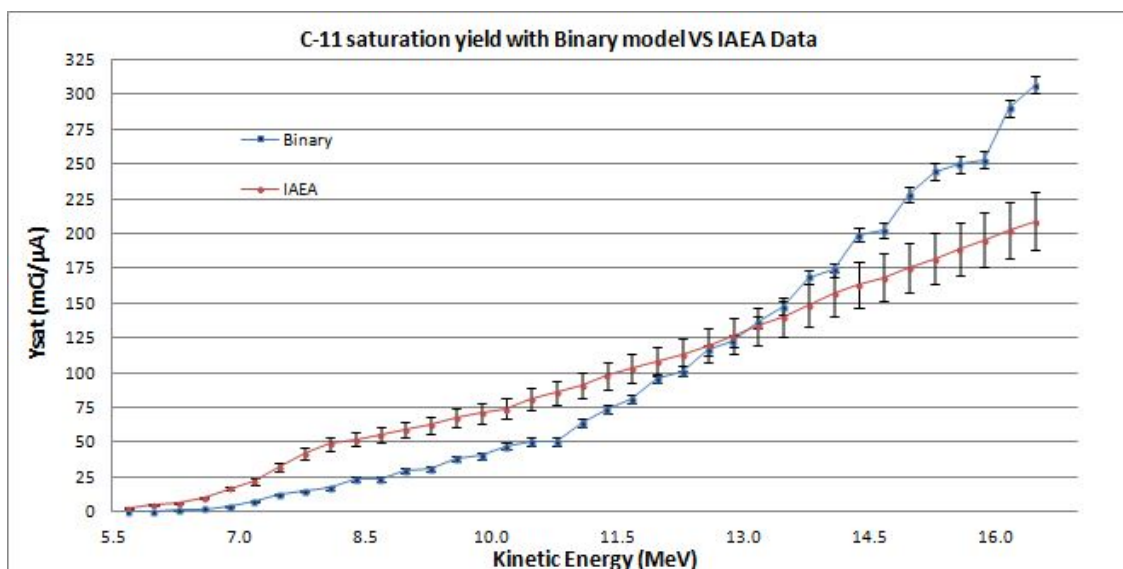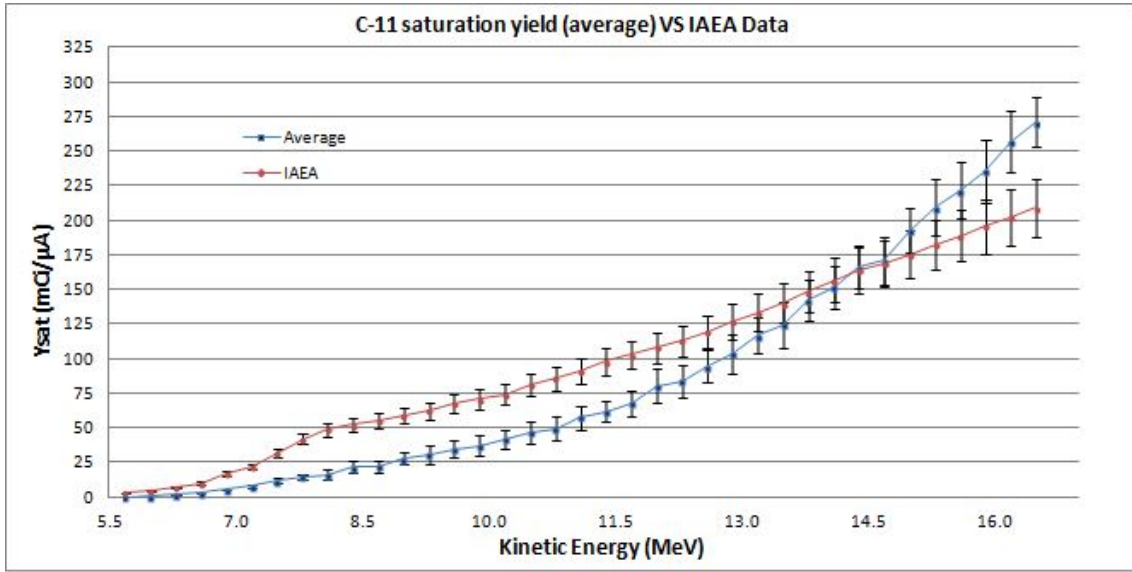Figure 5.8: Comparison between ^{11}C saturation yield as a function of energy, using Binary model, and IAEA data.

73

Figure 5.9: Comparison between ^{11}C saturation yield as a function of energy, using the average of the values obtained with Binary model, Precompound model with G4ChipsProtonInelasticXS and G4IonProtonCrossSection, and IAEA data.

As it can be seen from the plots, using any model of those mentioned, at low energies Geant4 underestimated the experimental saturation yield, while at higher energies it overestimated the IAEA data. The difference between the tested hadron inelastic models was the interval of energy in which this transition occur. The saturation yield provided by Precompound model with G4ChipsProtonInelasticXS was compatible, within the errors, with IAEA data between 15.0 MeV and 16 MeV, the values obtained by Precompound model with G4IonProtonCrossSection were consistent with IAEA data between 13.0 MeV and 15.5 MeV, while the Binary values were compatible between 12.0 MeV and 14.0 MeV.

For the energy range of our interest, the best result was provided by the Precompound model with G4ChipsProtonInelasticXS cross section class. Then it was chosen as model to use for the description of the hadron inelastic processes.

5.2.2 ^{11}C saturation yield using the full modeled target

The ^{11}C saturation yield obtained by Geant4, using the Precompound model with G4ChipsProtonInelasticXS, was, if the BEV and ^{11}C target were perfectly aligned, 176.5±1.9 mCi/μA, as it can be seen from the table 5.2. This value is about the 40% greater than the saturation yield obtained with the GE PETtrace cyclotron (125±13

mCi/μA), when the target was just cleaned. It was observed in several works that Monte Carlo simulations provide yield values greater than the experimental data [48, 49]. In our specific case, we consider that this difference is related to the fact that we measured the extracted activity, not the produced activity (it is likely that some of the produced isotopes get trapped in the target); moreover, with Geant4 we did not simulated thermodynamics and others effects, which may potentially reduce the saturation yield, such as:

- pressure in the target increases due to the heat produced during the irradiation, and, for this reason the front Havar^{TM} foil of the nitrogen chamber warps;

- the temperature in the target is not uniform, since the beam enters only from one side;

- there could be a radial gradient of temperature;

- the convective motions of the gas may produce small density gradients;

- an irradiation goes on for about 20 minutes, while we simulated individual instants;

- the electrostatic interactions between ions;

- the chemical reactions that will occur in the target due to ionizations caused by the proton beam.

Therefore, ^{11}C saturation yield was measured by modifying the angle between the BEV and ^{11}C target, shooting each time 1E7 protons.

This analysis was performed since the ^{11}C target, being relatively heavy, presses on the beam exit port and can gradually assume an inclination as time goes by. To avoid this kind of effect, in practice a support band was applied to balance the weight, as it can be seen from fig.5.10. However, it is generally possible that, if not specific precautions are taken, the target get slightly misaligned. We, then, modeled this situation in order to assess how much it affects the saturation yield.

The relative difference between the saturation yield at 0.0 deg and at 3.5 deg, as it can be seen from the table 5.2, depends on the model that was used (22% for the Precompound model with ChipsProtonInelasticXS cross section class, 33% for the Precompound model with IonProtonCrossSection, and 29% for the Binary model). The
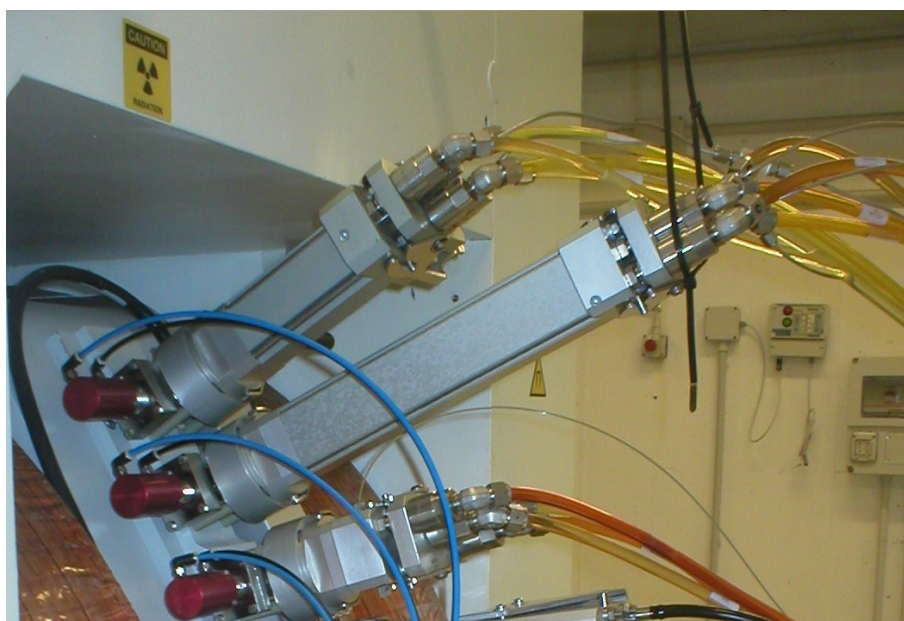
Figure 5.10: Image of the ^{11}C target (the longest one). It can be seen the support band that was applied to handle the weight of the target.

fact that this variation is not the same for the tested models, is a further proof of the importance of the choice of the model to use.

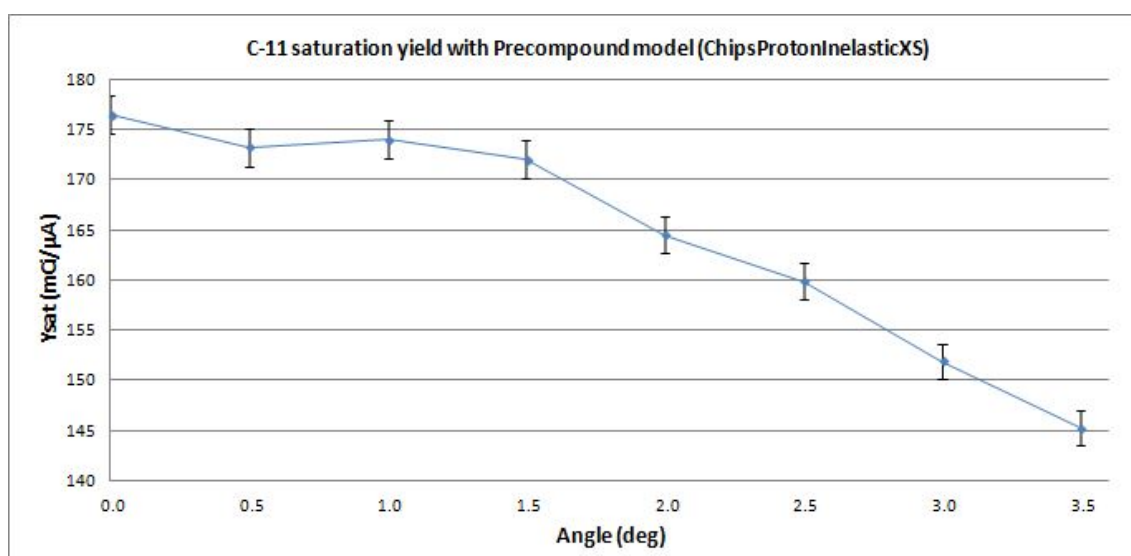In figure 5.11 the results for the Precompound model with ChipsProtonInelasticXS were plotted.

Figure 5.11: ^{11}C saturation yield as a function of the angle between the BEV and ^{11}C target, using the Precompound model with G4ChipsProtonInelasticXS cross section class.

Angle (deg)	ChipsProtonInelasticXS Y_{sat} (mCi/μA)	IonProtonCrossSection Y_{sat} (mCi/μA)	Binary Y_{sat} (mCi/μA)
0.0	176.5 $\pm$ 1.9	190.0 $\pm$ 2.0	224.0 $\pm$ 2.1
0.5	173.2 $\pm$ 1.9	184.1 $\pm$ 1.9	222.5 $\pm$ 2.1
1.0	174.0 $\pm$ 1.9	187.5 $\pm$ 2.0	216.4 $\pm$ 2.1
1.5	172.1 $\pm$ 1.9	182.8 $\pm$ 1.9	214.3 $\pm$ 2.1
2.0	164.5 $\pm$ 1.8	174.3 $\pm$ 1.9	208.4 $\pm$ 2.1
2.5	159.8 $\pm$ 1.8	162.4 $\pm$ 1.8	198.7 $\pm$ 2.0
3.0	151.9 $\pm$ 1.7	154.4 $\pm$ 1.8	187.9 $\pm$ 1.9
3.5	145.3 $\pm$ 1.7	142.6 $\pm$ 1.7	173.4 $\pm$ 1.8

Table 5.2: ^{11}C saturation yield as a function of the angle between the BEV and ^{11}C target, changing type of hadron inelastic model (Precompound with G4ChipsProtonInelasticXS, Precompound with G4IonProtonCrossSection, and Binary). The values were measured shooting 1E7 protons and errors, which are propagation of uncertainties related to the Poisson distribution, were added to measures.

As it can be seen from this figure, the saturation yield, using the Precompound model with G4ChipsProtonInelasticXS cross section class, was constant, within the statistical errors, for angles up to 1.5 deg, then it decreased. As a conclusion, proper preventive actions are advisable, in order to not incur in a misalignment greater than 1.5 deg.

5.3 Energy deposited in the aluminum target body

Using the model of the target previously described, we estimated the energy deposited in the lateral side of the target body. To this end, in the fig. 5.12 the energy deposited on the lateral side of the nitrogen chamber was represented as a function of the position along the axis parallel to this side. For comparison, in fig. 5.13 the energy deposited in the high-pressure nitrogen, with respect to the same projection, was represented.

Knowing the number and the average energy of the primary protons that enter in the nitrogen chamber, and measuring the total energy which was deposited in the lateral side of the chamber and in the nitrogen, it was evaluated the energy absorbed by all the lateral side (about 18% of the 1.5E4 mW/μA that enter in the nitrogen chamber), and in the nitrogen (about 79% of the 1.5E4 mW/μA that enter in the nitrogen chamber). The remaining 3% was energy deposited in the rear flange or relative to backscattering particles or photons that did not interact in the nitrogen chamber and diffuse in the environment.

As it can be seen, the maximum of deposited energy in the aluminum was shifted backward of about 5.5 cm with respect to the Bragg peak, and, instead, the energy peak in the aluminum was much more smoothed (FWHM$\approx$5 cm). Moreover, the maximum energy deposited in the nitrogen was greater than the maximum in the lateral side of the nitrogen chamber by a 5.7 factor.

Then we evaluated the energy deposited in the lateral side of the target body as a function of the azimuthal angle on a plane perpendicular to the lateral side and passing through the point in which the process occur. In the figure 5.14 an interference pattern, which were caused by the differences in the two perpendicular dimensions of the collimator slit and in the gaussian distributions of the perpendicular initial positions of the proton beam, was highlighted. As it can be seen from fig. 5.15, if the simulated beam is point-like, the interference patterns disappear.
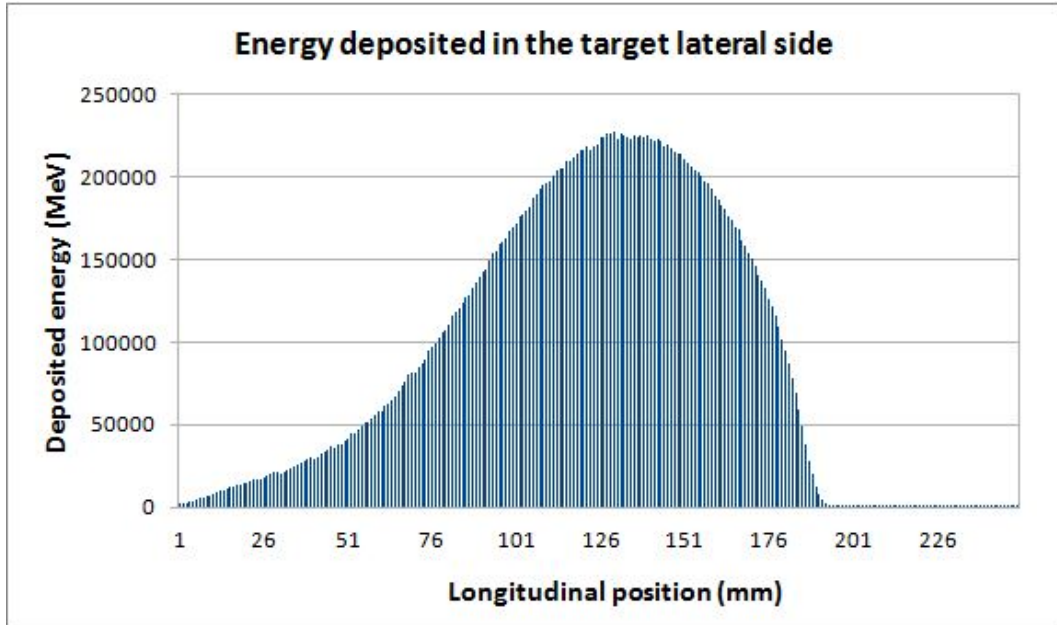
Figure 5.12: Energy deposited in the lateral side of the high-pressure nitrogen chamber as a function of the position along the axis parallel to this side. The plot was obtained by shooting 1E7 protons.
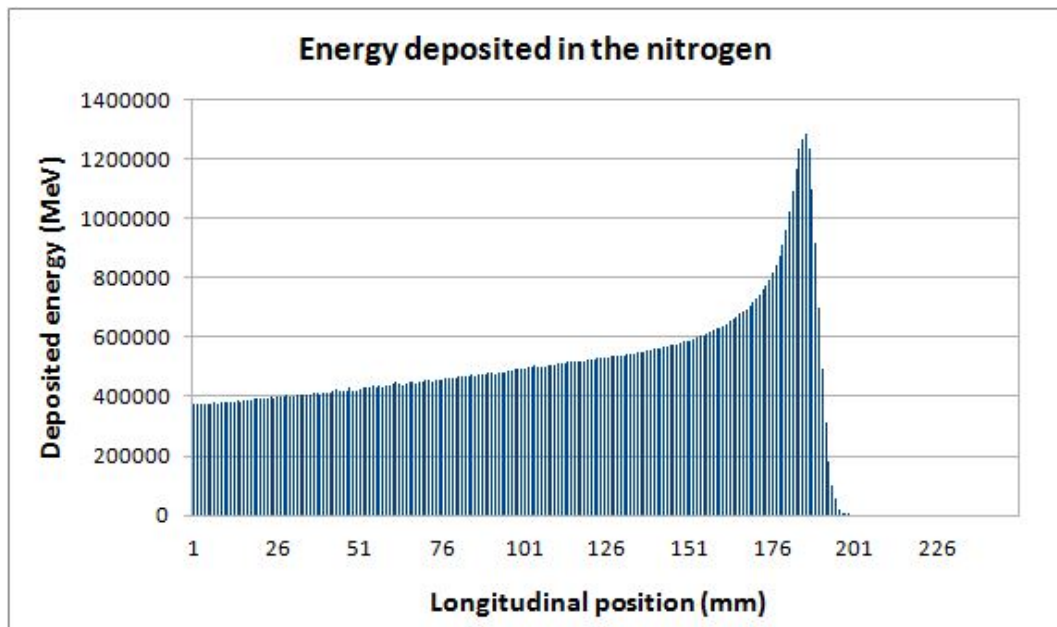

Figure 5.13: Energy deposited in the high-pressure nitrogen as a function of the position along the axis parallel to the lateral side of the nitrogen chamber. The plot was obtained by shooting 1E7 protons.
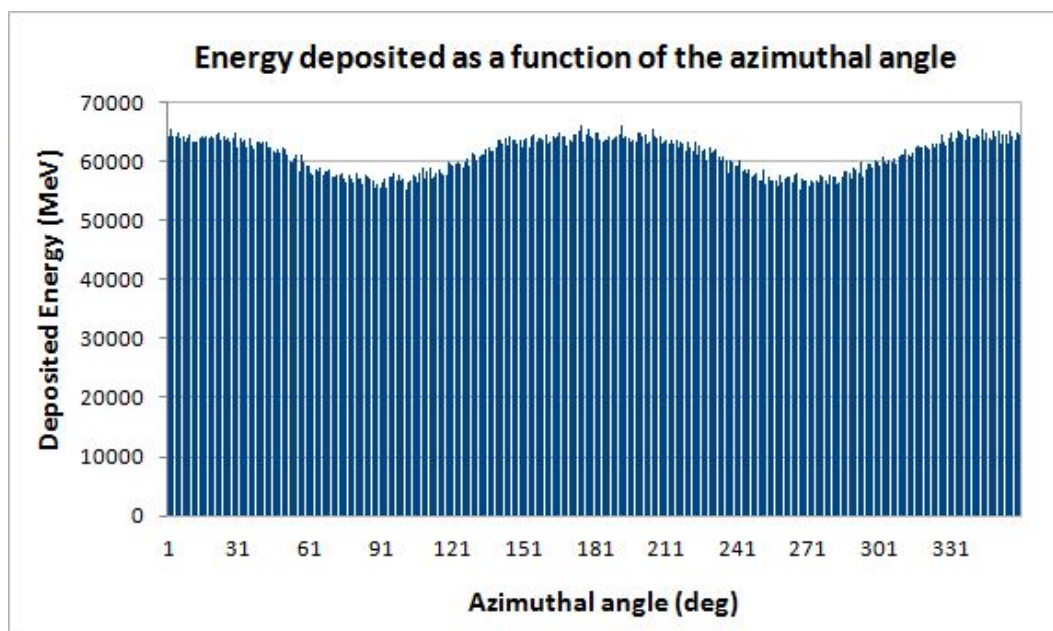
Figure 5.14: Energy deposited in the lateral side of the high-pressure nitrogen chamber as a function of the azimuthal angle on a plane perpendicular to the lateral side and passing through the point in which the process occur. The plot was obtained by shooting 1E7 protons.
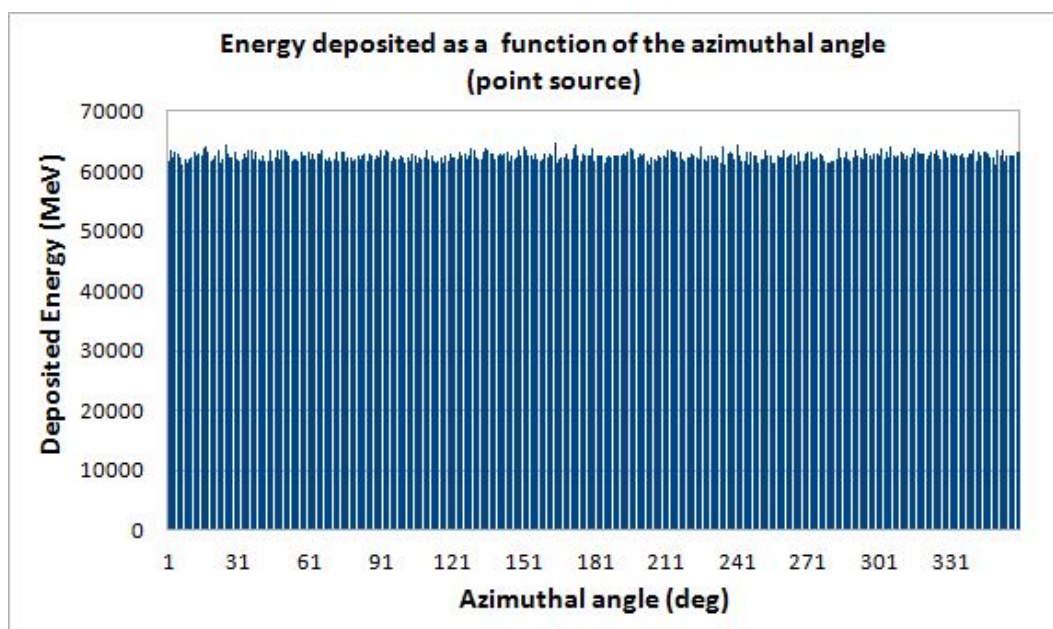

Figure 5.15: Energy deposited in the lateral side of the high-pressure nitrogen chamber as a function of the azimuthal angle on a plane perpendicular to the lateral side and passing through the point in which the process occur, when the proton source was point-like simulated. The plot was obtained by shooting 1E7 protons.

Figure 5.16 shows a scoring mesh concerning the energy deposited in a circular layer of 0.5 cm of thickness, surrounding the nitrogen chamber, by 3E7 protons, when the target was aligned. The scoring mesh was divided in 150×38 bins in order to have almost square pixels ($1.\bar{6}×1.\bar{6}$ mm^2). The estimated energy deposited in a element of the area of maximum absorption was of 3.3E4 MeV: the 0.007% of the total energy of the proton beam was deposited in each of these pixels. Assuming that this energy was deposited in a second and converting the energy in Joule, it was seen that 119 J were locally absorbed in a typical irradiation time of 20 minutes. Since, in practice, an average of 4 irradiations per week ($\approx$ 200 per years) are performed, this means that approximately 50 kJ of energy are deposited in 2 years on the most irradiated pixels of the surface surrounding the nitrogen chamber. This is consistent with the progressive deterioration of the inner surface of the target with time, leading to the need of cleaning and rebuilding the target about every two years.
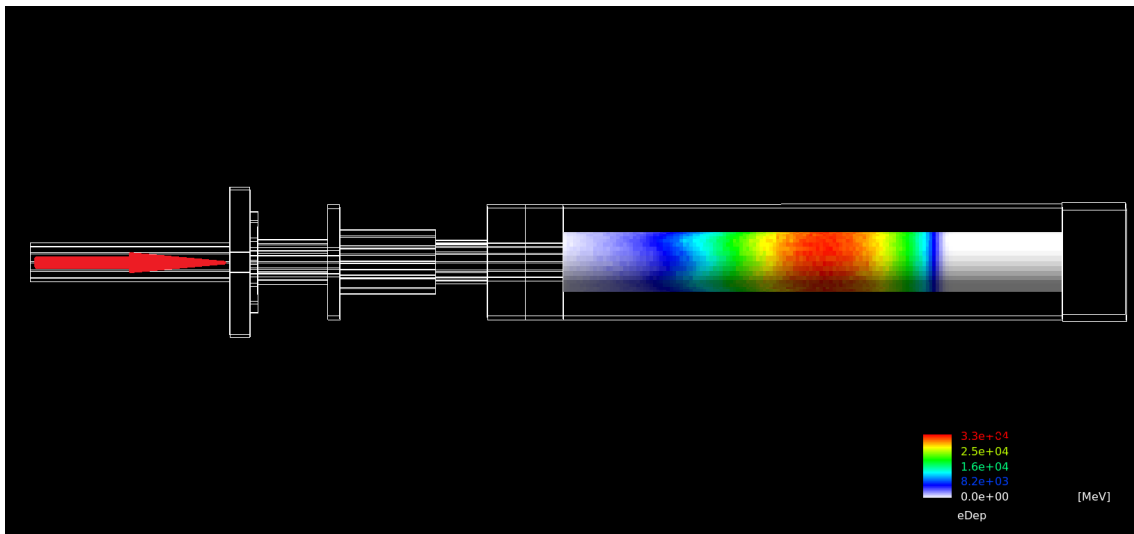

Figure 5.16: Scoring mesh of the energy deposited in 0.5 cm of the aluminum lateral side of the nitrogen chamber. The mesh, that was graphically superimposed on the simulated geometry, was obtained by shooting 3E7 protons. The red arrow specifies the direction of the proton beam.

If we modify the angle between the BEV and ^{11}C target, in order to reproduce the misalignment of the target, the position of the region of maximum absorption, clearly, changes both in the nitrogen and in the lateral side, together with the maximum value of deposited energy.

As it can be seen from fig. 5.17, the region of maximum absorption in the lateral side of the nitrogen chamber was increasingly back shifted by enhancing the misalignment
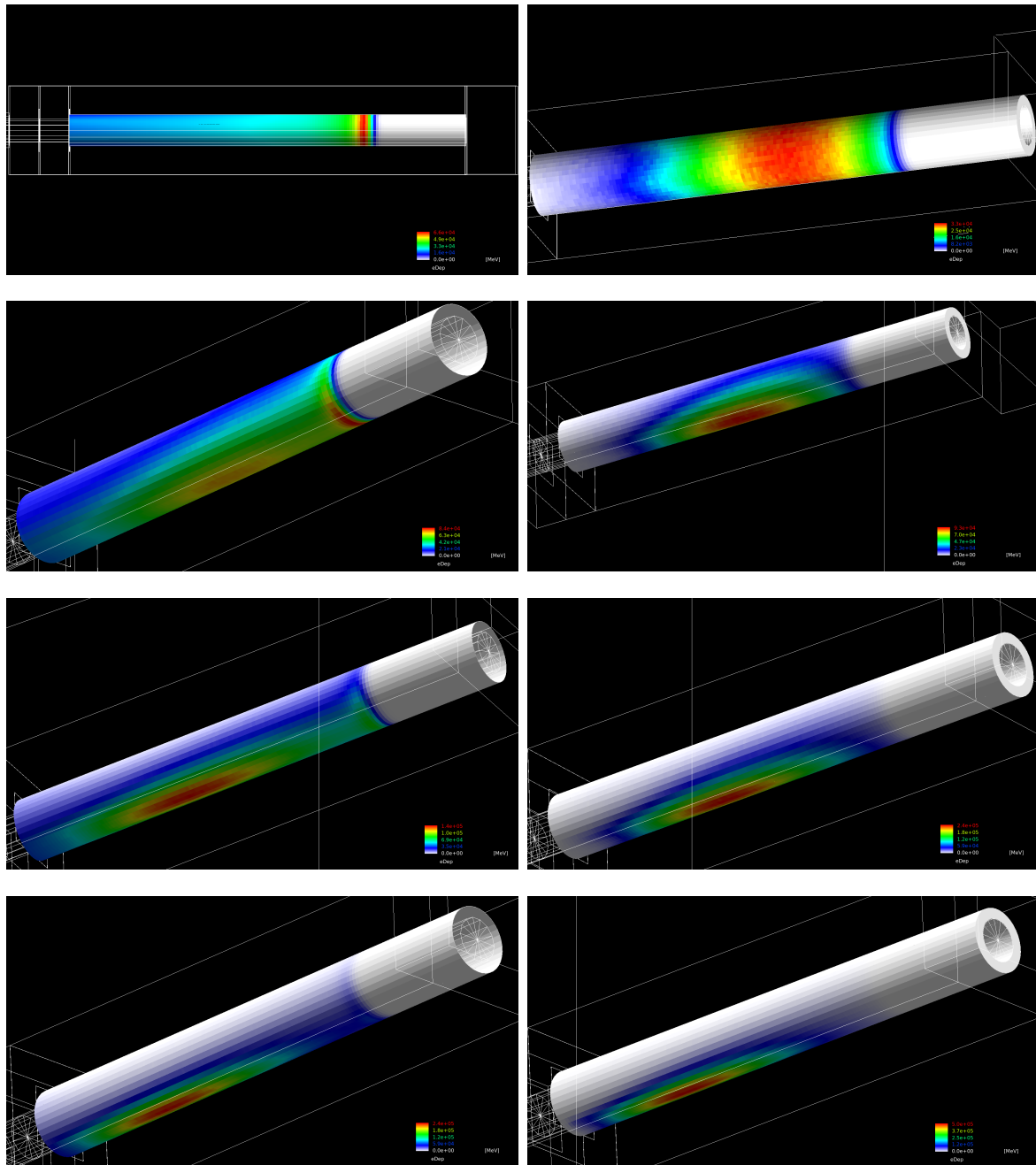
Figure 5.17: On the left, scoring meshes, obtained by shooting 1E7 protons, in which the energy deposited in the nitrogen and in the lateral side of the nitrogen chamber, were represented. On the right, scoring meshes, obtained by shooting 3E7 of protons, in which the energy deposited only in the lateral side of the nitrogen chamber, were represented. In the first row are shown the meshes which were obtained when the target was aligned. In the second row the meshes were achieved with an angle of 1.0 deg between the BEV and ^{11}C target, in the third the angle was of 2.0 deg, and in the fourth of 3.0 deg. The mesh were graphically superimposed on the simulated geometry.

angle. This region was also increasingly sharped and positioned in the lower part of the target, where the protons collided. Moreover, with an angle of 0.5 deg between the BEV and ^{11}C target, the maximum energy absorbed by the pixels of the surface surrounding the nitrogen chamber increased up to 3 times in respect to the perfectly aligned system, and, for a misalignment of 3.5 deg, the energy adsorbed reached 15 times the value of the aligned system. As a consequence, the foreseeable operational time of the target is expected to be reduced of a factor equal to the increase in the energy deposited in the region of maximum absorption: this means, for a misalignment 0.5 deg, about 8 months and a half of operational time, and, for a misalignment of 3.5 deg, just a month and a half of operational time.

Up to 1.0 deg, then, the energy deposited in nitrogen, in the Bragg peak area, was higher than that deposited in the lateral side, but for greater angles this was no longer true.

5.4 Other activation processes

During the irradiation, ^{11}C is not the only type of radionuclide which was produced. Other activation processes occurred, during the irradiation, both in the high-pressure nitrogen and in the lateral side of the nitrogen chamber.

The radionuclides, which were produced in the nitrogen in addition to the ^{11}C nuclei, are:

1. ^{13}N, which decades $\beta+$ in ^{13}C ($T_{1/2}$=9.97 min). The ^{13}N simulated saturation yield was the 8.90±0.04 % of the ^{11}C saturation yield. It was produced by (p,d) and (p,np) reactions on the ^{14}N nuclei.

2. ^{7}Be, which decades by electron capture in ^{7}Li ($T_{1/2}$=53.22 d). The ^{7}Be simulated saturation yield was the 0.292±0.006 % of the ^{11}C saturation yield. It was produced by (p,2α) reactions on the ^{14}N nuclei.

3. ^{15}O, which decades $\beta+$ in ^{15}N ($T_{1/2}$=2.037 min). The ^{15}O simulated saturation yield was the 0.167±0.005 % of the ^{11}C saturation yield. It was produced by (p,n) reactions on the ^{15}N nuclei.

4. ^{17}F, which decades $\beta+$ in ^{17}O ($T_{1/2}$=64.5 s). The ^{17}F simulated saturation yield

was the 0.044 ± 0.002 % of the ^{11}C saturation yield. It was produced by (p,γ) reactions on the ^{16}O nuclei.

5. ^{18}F, which decades β+ in ^{18}O (T$_{1/2}$=109.77 min). The ^{18}F simulated saturation yield was the 0.0005 ± 0.0002 % of the ^{11}C saturation yield. It was produced by (p,n) reactions on the ^{18}O nuclei.

The nuclides which, instead, were produced in the lateral side of the chamber, are:

1. ^{28}Si (stable isotope), which was produced by (p,γ) reactions on the ^{27}Al nuclei.

2. ^{28}Al, which decades β- in ^{28}Si (T$_{1/2}$=2.24 min). The ^{28}Al simulated saturation yield was the 0.275 ± 0.006 % of the ^{11}C saturation yield. It was produced by (n,γ) reactions on the ^{27}Al nuclei.

3. ^{27}Si, which decades β+ in ^{27}Al (T$_{1/2}$=4.2 s). The ^{27}Si simulated saturation yield was the 0.0716 ± 0.0029 % of the ^{11}C saturation yield. It was produced by (p,n) reactions on the ^{27}Al nuclei.

All these results were provided by shooting 1E9 protons. The errors associated to these data are derived by propagating the uncertainties related to the Poisson distribution.

The ^{15}O and ^{17}F nuclei quickly decay and are not detectable in the target gas at the end of the production. ^{18}F nuclei in gas phase bind together, forming ^{18}F$_2$ molecules. These are highly chemically reacting and it is well known that strongly stick to the chamber walls and cannot be extracted from the target. However, the silicon produced in the lateral side of the nitrogen chamber, although it was produced in small quantities, may cause alteration in the electrical and thermal properties of the material chosen to contain the gas mixture.

The nuclear reaction involved for the ^{7}Be production was, originally, described by Jacobs et al.[50]. It has a threshold at 11.3 MeV and is effectively possible in the case of cyclotron for biomedical use, like the PETtrace. Indeed, the presence of ^{7}Be nuclei, that due to their long half-life accumulate in the nitrogen chamber, was also confirmed for our cyclotron, during the cleaning phase of the inner walls of the target, by means of a HPGe gamma spectrometry system, installed at the Bologna University Hospital "S. Orsola-Malpighi".[51]

The produced ^{13}N do not affect the radiopharmaceuticals synthesis, since the nuclides are separated before they are used, but it is relevant in the measurements of the produced activity, in the case they are conducted before the nuclides are separated.
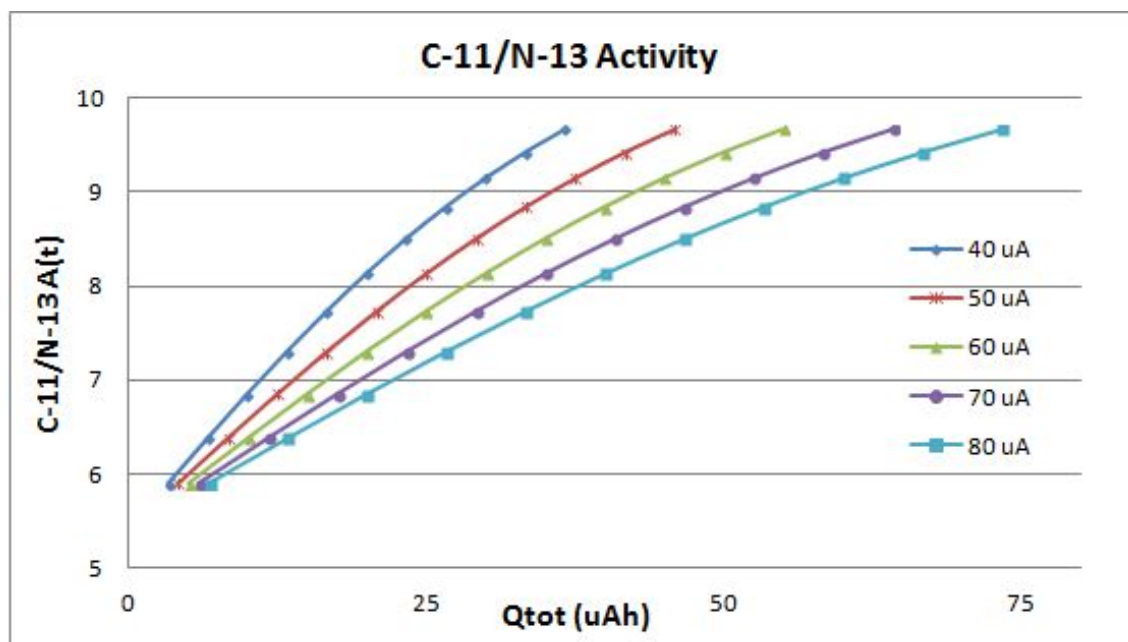

Figure 5.18: Ratio of the ^{11}C and ^{13}N activities as a function of the total charge of the beam, for different values of the beam current.

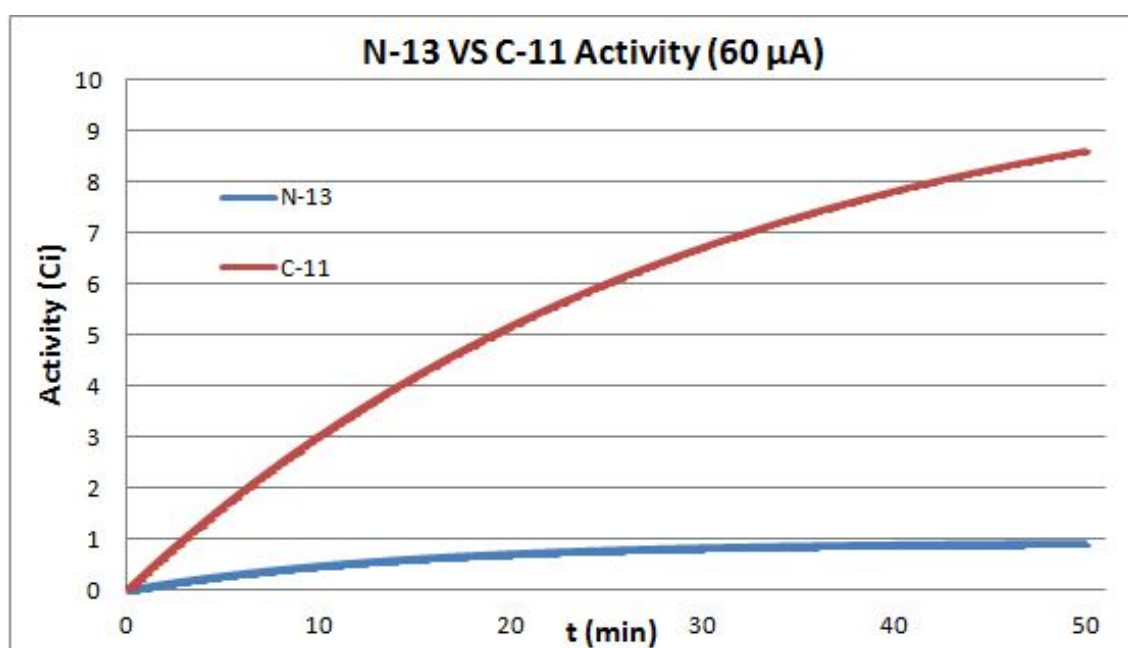Figure 5.19: Comparison between the ^{11}C and ^{13}N activities in the target as a function of the time, with a beam current of 60 μA.

Therefore, the ratio of the ^{11}C and ^{13}N activities as a function of the total charge of the beam, using the saturation yields obtained from the simulation, was evaluated for different beam currents (40, 50, 60, 70, 80 μA), in order to assess the combination with the largest ^{11}C/^{13}N ratio. As it can be seen in fig. 5.18, for the same total charge, the highest ratio was obtained for the lower beam current (40 μA), i.e. for a high irradiation time with a a low beam current.

As example, figure 5.19 shows, on the same plot, the activities of ^{11}C and ^{13}N in the target as function of the time, if the proton current is of 60 μA.

Conclusions

The developments of increasingly advanced instrumentation and the availability of ever more powerful computing systems have led to an increasing use of *Monte Carlo* techniques in Medical Physics, both in diagnostics and in therapy, for the design and optimization of several instrumentation in this field, including radiation detectors, imaging and radio-protection devices.

In this thesis, which was conducted at the Medical Physics unit of the Bologna University Hospital "S. Orsola-Malpighi", I developed a Monte Carlo model of the target, by the use of Geant4 (a *general purpose* Monte Carlo toolkit developed at CERN), for routine production of ^{11}C of the GE-PETtrace biomedical cyclotron.

The model includes the main geometrical details of the target, such as the collimator, the high-pressure helium cooling chamber and the Havar foils. The proton beam was modeled using factory data and experimental measurements, such as *paper burn*s and the proton current detected on the collimator. In an initial set of simulations, aimed to find the optimal parameters of the Physics List to be used, a simplified geometry was utilized. Standard electromagnetic processes were activated for the particles involved, while for inelastic hadronic processes, as a result of an in-depth analysis, the precompound model was used. Results were analyzed using the ROOT toolkit.

The model was validated through known and experimental physical parameters in order to assess its accuracy. The model of the target establishes, in fact, a powerful tool for a number of applications and studies regarding the performance and behavior of the target during irradiation.

For validation, the beam energy at the chamber entry point, the mean range of the beam in the chamber and Bragg peak position were compared with results obtained with SRIM. The simulated saturation yield of ^{11}C nuclei was compared with both IAEA database and our experimental data, and was assessed also as a function of the tilting angle of the target body with respect to the proton beam, which may arise due to

Conclusions

the weight of the target and its mounting position. Other activation processes which occur during the irradiation in the high-pressure nitrogen were estimated. The energy absorbed and the activation processes on the internal surface of the target chamber, parameters useful to explain degradation of the performance, were also studied.

The results for the beam energy at the nitrogen chamber entry point (15.22±0.01 MeV), the mean range of the protons in the high-pressure nitrogen (18.83±0.01 cm) and the Bragg peak position (18.60±0.05 cm) are in good agreement with the values measured with SRIM. ^{11}C saturation yield obtained with simulations was 176.5±1.9 mCi/μA, +40% of the experimental results. This is corresponding to what normally is obtained with MC simulations compared to experimental results, which take into account chemical and thermodynamic processes.

Therefore, the model was used for the evaluation of the parameters of interest relating, in particular, to the degradation of the target as time goes by. It was evaluated, for example, that the 18% of the 1.5E4 mW/μA that enter in the nitrogen chamber was absorbed by the lateral inner walls of the target. Furthermore, about 50 kJ of energy are deposited in 2 years of typical irradiations in each $1.\bar{6}{\times}1.\bar{6}$ mm^2 pixel of the inner lateral walls of the target in the region of maximum absorption.

Increasing the angle between the BEV and ^{11}C target, the maximum value of energy deposited in each pixel of the region of maximum absorption increased (up to a 15 factor for 3.5 deg of misalignment). This involves that the foreseeable operational time of the target is expected to be reduced of a factor equal to the increase in the energy deposited in the region of maximum absorption (from about 2 years to about one and half month or less, for 3.5 deg of misalignment). Moreover, the saturation activity was not affected significantly for tilting angles below 1.5 degrees, while for example at 3.0 degrees we observed a reduction of about 16%.

It was seen that several nuclides were produced in the wall of the nitrogen chamber, such as ^{28}Al, ^{27}Si, ^{28}Si (stable), and in the gas, such as ^{7}Be and ^{13}N. The produced nuclides, although were produced in small quantities, may cause, both with the mentioned thermal stress, a deterioration in the material of the wall of the nitrogen chamber which could lead to a yield decrease.

The developed model provided satisfactory results regarding both electromagnetic and hadron inelastic interactions of protons. Some discrepancies obtained, in comparison to the expected data, suggests that further improvements and tuning in the Geant4

hadronic models may be required. In the future versions of Geant4, such as the upcoming 10.1 release, probably, will be available new physics libraries, which will allow a more accurate modeling of hadronic interactions at low energies. It must also be noted that the quite lower experimental yield is to be attributed to (mostly) thermodynamics effects that were not modeled with Geant4.

In conclusion, the model, to the best of our knowledge the first of this type to be developed, establishes a powerful tool for the comprehension of material behavior in the target irradiation, for supporting the assessment and optimization of new targetry, and to assess performance of targets over time.

Conclusions

Bibliography

[1] M. Marengo; "La fisica in medicina nucleare", Patron Editore, Bologna 2001.

[2] Data available on IAEA website, "http://www.iaea.org".

[3] C.L. Melcher; "Scintillation Crystals for PET", 2000.

[4] L. Motz, J.H. Weaver; "La storia della fisica", Cappelli, Bologna 1991.

[5] K. Strijckmans; "The isochronous cyclotron: principles and recent developments", Computerized Medical Imaging and Graphics 25(2001) pp. 69-78.

[6] PETtrace Service Manual – Accelerator-.

[7] B.F. Milton; "Commercial Compact Cyclotrons in the 90's", 14h International Conference on Cyclotron and their Application, NSCL# 3429.

[8] R. Finn, D. Schlyer; "Production considerations for the *classical* PET nuclides".

[9] S.K. Krane; "Introductory Nuclear Physics", Wiley, 1987.

[10] E. Segrè; "Nuclei e Particelle", ed. Zanichelli, Bologna.

[11] A. Davydov; "Teoria del nucleo atomico", Zanichelli, 1966.

[12] NIST website, "http://www.nist.gov".

[13] N. Metropolis; "The beginning of the Monte Carlo method", Los Alamos Science, 1987.

[14] M.H. Kalos and A.P. Whitlock; "Monte Carlo Methods, Wiley-VCH", 2008.

[15] C. Bishop; "Pattern Recognition and Machine Learning", Springer, 2006.

[16] M.R. Neal; "Slice Sampling", Annals of Statistics 31, 2003.

Bibliography

[17] Aalto University, N. Hyvönen; "Computational methods in inverse problems", twelfth lecture.

[18] G. Cowan; "Monte Carlo Techniques", Review of Particle Physics 33, Particle Data Group, 2008.

[19] Walck; "Handbook on Statistical Distributions for experimentalists", 1996.

[20] C.P. Robert and G .Casella; "Monte Carlo Statistical Methods" (second edition), New York: Springer-Verlag, 2004.

[21] Zaidi; "Relevance of accurate Monte Carlo modeling in nuclear medical imaging", Medical Physics 26 n.4, 1999.

[22] M. Ljungberg, S.-E. Strand and M.A. King; "Monte Carlo calculations in nuclear medicine: Applications in diagnostic imaging", IOP Publishing, Bristol, 1998.

[23] I. Buvat and I. Castiglioni; "Monte Carlo simulations in SPET and PET", Q J Nucl Med 46: 48-61, 2002.

[24] H. Zaidi, A.H. Scheurer and C. Morel; "An object-oriented Monte Carlo simulator for 3D cylindrical positron tomographs", Computer Methods and Programs Biomedicine 58: 133-145, 1999.

[25] M.L. Mangano and T.J. Stelzer; Ann. Rev. Nucl. Part. Sci. Vol.55: 555-558, 2005.

[26] M.A. Dobbs et al.; hep-ph/0403045.

[27] T. Sjöstrand, S. Ask, J.R. Christiansen, R. Corke, N. Desai, P. Ilten, S. Mrenna, S. Prestel, C.O. Rasmussen, P.Z. Skands; "An Introduction to PYTHIA 8.2", LU TP 14-36, 2014.

[28] E.E. Boos, M.N. Dubinin, V.F. Edneral, V.A. Ilyin, A.P. Kryukov, A.E. Pukhov, A.Ya. Rodionov, V.I. Savrin, D.A. Slavnov, A.Yu. Taranov; "CompHEP - computer system for calculation of particle collisions at high energies", SINP MSU report 89-63/140, 1989;

[29] Nelson et al.; "The EGS4 Code System", SLAC-R-265, 1985.

[30] W.R. Nelson, H. Hirayama, and D.W.O. Rogers; "The EGSnrc Code System: Monte Carlo Simulation of Electron and Photon Transport", SLAC-265, 1985.

[31] D.W.O. Rogers, B. Walters, I. Kawrakow; "BEAMnrc users manual", NRCC Report PIRS-0509(A)revL, 2011.

[32] X-5 Monte Carlo Team; "MCNP - A General N-Particle Transport Code, Version 5", Volume I: Overview and Theory, LA-UR-03-1987, 2003, updated 2005.

[33] F. Salvat, J.M. Fernández-Varea, J. Sempau; "PENELOPE – A Code System for Monte Carlo Simulation of Electron and Photon Transport", Workshop Proceedings Issy-les-Moulineaux, France, 7-10 July 2003.

[34] A. Ferrari, A. Fassò, J. Ranft, P.R. Sala; "FLUKA: a multi-particle transport code", CERN 2005-10 (2005), INFN/TC_05/11, SLAC-R-773.

[35] G. Battistoni, S. Muraro, P.R. Sala, F. Cerutti, A. Ferrari, S. Roesler, A. Fassò, J. Ranft; "The FLUKA code: Description and benchmarking", Proceedings of the Hadronic Shower Simulation Workshop 2006, Fermilab 6-8 September 2006, M. Albrow, R. Raja eds., AIP Conference Proceeding 896, 31-49; 2007.

[36] S. Agostinelli, J. Allison, K. Amako, J. Apostolakis, H. Araujo, P. Arce, M. Asai, D. Axen et al.; "Geant4—a simulation toolkit", Nuclear Instruments and Methods in Physics Research Section A: Accelerators, Spectrometers, Detectors and Associated Equipment 506 (3): 250, 2003.

[37] J. Allison, K. Amako, J. Apostolakis, H. Araujo, P. Arce Dubois, M. Asai, G. Barrand, R. Capra, S. Chauvie, R. Chytracek, G.A.P. Cirrone, G. Cooperman, G. Cosmo, G. Cuttone, G.G. Daquino, M. Donszelmann, M. Dressel, G. Folger, F. Foppiano, J. Generowicz, V. Grichine, S. Guatelli, P. Gumplinger, A. Heikkinen, I. Hrivnacova, A. Howard, S. Incerti, V. Ivanchenko, T. Johnson et al.; "Geant4 developments and applications", IEEE Transactions on Nuclear Science 53: 270, 2006.

[38] Geant4 Collaboration; "Geant4 User's Guide for Application Developers", "http://geant4.web.cern.ch/geant4/UserDocumentation/UsersGuides/ForApplicationDeveloper/html/index.html".

Bibliography

[39] J.F. Ziegler, J.P. Biersack and M.D. Ziegler; "SRIM - The stopping and range of ions in matter", SRIM Co, 2008.

[40] J.F. Ziegler, M.D. Ziegler, and J.P. Biersack; "SRIM - The stopping and range of ions in matter", Nuclear Instruments and Methods in Physics Research B 268 1818–1823, 2010.

[41] J. Tuli; "Evaluated Nuclear Structure Data File", BNL-NCS-51655-Rev87, 1987.

[42] http://geant4.cern.ch/support/proc_mod_catalog/models/hadronic/BinaryCascade.html

[43] http://geant4.cern.ch/support/proc_mod_catalog/models/hadronic/Precompound.html

[44] SLAC Geant4 team; "http://www-public.slac.stanford.edu/geant4/".

[45] http://geant4.cern.ch/support/proc_mod_catalog/models/hadronic/BertiniCascade.html

[46] R. Brun and F. Rademakers; "ROOT - An Object Oriented Data Analysis Framework", Proceedings AIHENP'96 Workshop, Lausanne, Sep. 1996, Nucl. Inst. & Meth. in Phys. Res. A 389 (1997) 81-86. See also http://root.cern.ch/.

[47] IAEA-TECDOC-1211 "Charged particle cross-section database for medical radioisotope production: diagnostic radioisotopes and monitor reactions".

[48] A. Infantino, M. Marengo, S. Baschetti, G. Cicoria, V. Longo Vaschetto, G. Lucconi, P. Massucci, S. Vichi, F. Zagni, M. Mostacci; "Accurate Monte Carlo modeling of cyclotrons for optimization of shielding and activation calculation in the biomedical field", Radiation Physics and Chemistry, Manuscript submitted for publication, 2014.

[49] L.M. Oranj, T. Kakavand, M. Sadeghi, M.A. Rovias; "Monte Carlo FLUKA code simulation for study of ^{68}Ga production by direct proton-induced reaction", Nuclear Instruments and Methods in Physics Research A 677 (2012) 22-24.

[50] W.W. Jacobs, D. Bodansky, D. Chamberlin, D.L. Oberg; "Production of Li and B in proton and alpha-particle reactions on ^{14}N at low energies", Physical Review C, vol.9, no.6, June 1974.

[51] J. Ledesma, G. Cicoria, K. Solanki, E. Noya,S. Boschi and M. Marengo; "Radiation safety issues in the maintenance of cyclotron targets for the production of ^{11}C".